
ORIGINAL ARTICLE

Supervised machine learning to estimate instabilities in chaotic systems: estimation of local Lyapunov exponents

Daniel Ayers¹ | Jack Lau² | Javier Amezcua¹ |
Alberto Carrassi^{1,3} | Varun Ojha²

¹Department of Meteorology and NCEO,
University of Reading, Reading, UK

²Department of Computer Science,
University of Reading, Reading, UK

³Department of Physics and Astronomy
"Augusto Righi", University of Bologna, Italy

Correspondence

Daniel Ayers
Email: d.ayers@pgr.reading.ac.uk

Funding information

UK Engineering and Physical Sciences
Research Council, Grant Number:
EP/N509723/1; UK National Centre for
Earth Observation Grant Number:
NCEO02004; Schmidt Futures.

In chaotic dynamical systems such as the weather, prediction errors grow faster in some situations than in others. Real-time knowledge about the error growth could enable strategies to adjust the modelling and forecasting infrastructure on-the-fly to increase accuracy and/or reduce computation time. For example one could change the spatio-temporal resolution of the numerical model, locally increase the data availability, etc. Local Lyapunov exponents are known indicators of the rate at which very small prediction errors grow over a finite time interval. However, their computation is very expensive: it requires maintaining and evolving a tangent linear model, orthogonalisation algorithms and storing large matrices. In this study, we investigate the capability of supervised machine learning to estimate the imminent local Lyapunov exponents, from input of current and recent time steps of the system trajectory, as an alternative to the classical method. Thus machine learning is not used here to emulate a physical model or some of its components, but "non intrusively" as a complementary tool. Specifically, we test the accuracy of four popular supervised learning algorithms: regression trees, multi-layer perceptrons, convolutional neural networks and long short-term memory networks. Experiments are conducted

on two low-dimensional chaotic systems of ordinary differential equations, the Lorenz 63 and the Rössler models. We find that on average the machine learning algorithms predict the stable local Lyapunov exponent accurately, the unstable exponent reasonably accurately, and the neutral exponent only somewhat accurately. We show that greater prediction accuracy is associated with local homogeneity of the local Lyapunov exponents on the system attractor. Importantly, the situations in which (forecast) errors grow fastest are not necessarily the same as those where it is more difficult to predict local Lyapunov exponents with machine learning.

KEYWORDS

supervised machine learning, local Lyapunov exponents, numerical modelling, chaos

1 | INTRODUCTION

Weather and climate are well known exemplars of chaotic dynamical systems. These systems exhibit extreme sensitivity to initial conditions, meaning that initial condition errors are subject to (on average) exponential growth until they reach saturation (Ghil and Lucarini, 2020). The rate and the characteristic of such growth, however, is highly state dependent (Lighthill et al., 1986; Vannitsem, 2017). As a consequence, although chaotic systems have a finite predictability horizon (about 2 weeks for the atmosphere, see *e.g.* Holton and Hakim (2013)), the best estimate of prediction error growth fluctuates in size along with the system's evolution, as the system goes through periods of lower or higher predictability. For example, the short-term predictability of the atmosphere depends on the weather regime present at a given time (see, *e.g.* Palmer, 1996). Understanding the nature of error growth is essential to characterising a system, and to enable better prediction. In an ideal setting where the degree of predictability of the system is known in real-time, it may be possible and beneficial to take adaptive measures. For instance, a local decrease of predictability may be counteracted by increasing the time- or space-resolution of the model computation or the ensemble size in the context of ensemble-based data assimilation or probabilistic forecasting. Conversely, in areas of high predictability, one can save computational resources (and thus energy consumption) by reducing the time- or space-resolution or the ensemble size. In this study we investigate the potential of machine learning (ML) methods (Bishop, 1995; Hastie et al., 2009) to provide such an ideal setting, that is, to provide a real-time estimation of the system's local predictability.

The mathematical theory of dynamical systems has long been the backbone to understand and quantify predictability in deterministic chaotic systems. This is commonly done by studying the instability properties of the solution, *i.e.* by analysing the linearised dynamics of small perturbations: the tangent space evolution of these "small" perturbations are taken as proxies of the dynamics of unknown initial condition errors (Ott, 2002). In this context, Lyapunov exponents (LEs) are well-established quantities that measure the asymptotic rates of error growth for a set of infinitesimally small errors that capture all directions of phase space (Pikovsky and Politi, 2016). In practice, they

measure the average growth of small finite errors over long periods of time. The spectrum of LEs is characteristic of each given dynamical system. Lyapunov exponents, and their corresponding Lyapunov vectors (LVs), have been exploited in geosciences for more efficient uncertainty quantification in data assimilation (e.g., Palatella et al., 2013; Albarakati et al., 2021; Carrassi et al., 2022), or for initialising probabilistic predictions (e.g., Toth and Kalnay, 1997; Buizza, 2019; Vannitsem and Duan, 2020). The LE spectrum can also be used to calculate other characteristic properties of a system, such as the Kolmogorov-Sinai entropy, measuring the rate of information loss (Sinai, 2009), or the Kaplan-Yorke attractor dimension (Kaplan and Yorke, 1979).

The LEs are calculated as an average of finite-time Lyapunov exponents which are here referred to as *local Lyapunov exponents*, LLEs (Benettin et al., 1980b,a; Kuptsov and Parlitz, 2012). Whereas LEs provide “global” information about the average growth of small perturbations in the system, the LLEs describe “local” growth rates along a finite-time section of the trajectory. Notably, the LLEs show the heterogeneity of the instabilities in phase space: the fluctuation of the local dynamical stability around the asymptotic value as the system state varies (Sandri, 1996; Pikovsky and Politi, 2016). This makes the LLEs ideal quantities to measure the local degree of predictability, yet a bottleneck for their real-time use in operational scenarios is the huge computational cost. Computational cost grows quickly with the system’s dimension making it prohibitive even for moderate size models, let alone for models as large as those currently used in numerical weather predictions ($\mathcal{O}(10^9)$ dimensions). Using the standard method (Benettin et al., 1980b,a; Kuptsov and Parlitz, 2012; Pikovsky and Politi, 2016), calculating the LLEs and LEs involves computing a long trajectory of the system (including a spin-up needed to ensure the solution has reached the model attractor), propagating perturbations (as many as the number of desired LLEs) with the tangent linear model (i.e., the resolvent of the model Jacobian), and then repeatedly performing a process of orthogonalisation (e.g. using a QR decomposition algorithm).

Avoiding the need for such a costly computation whilst attaining an estimate of the LEs or LLEs has thus great relevance. In their recent work, Chen et al. (2021) show how the outcomes of properly tuned data assimilation experiments can reveal the first LE as well as the Kolmogorov-Sinai entropy of the underlying dynamical model. The present work also seeks to avoid the cost of classical calculation methods, albeit only when time is critical. We investigate the feasibility of using certain ML methods (Bishop, 1995; Hastie et al., 2009) to estimate the LLEs based only on information from the system’s solution. Our focus is on supervised learning, which uses a data set of input-output pairs. The targets, i.e. the desired outputs, are LLEs calculated using the classical method of evolving perturbations via the tangent linear model and orthogonalising. In this way, the cost of such methods is paid during the training phase of the ML method, and is avoided when making predictions.

In the area of weather and climate forecasting, supervised learning has been used for various purposes (see e.g., Reichstein et al., 2019; Rasp et al., 2020; Chantry et al., 2021; Düben et al., 2021, and references therein). These include: (i) to emulate the full dynamics of a system (Pathak et al., 2017, 2018; Fablet et al., 2018; Nguyen et al., 2019; Brajard et al., 2020; Patel et al., 2021; Schultz et al., 2021; Sonnewald et al., 2021), (ii) to improve a physics-based model with data-driven correction or parameterisation (O’Gorman and Dwyer, 2018; Rasp et al., 2018; Bolton and Zanna, 2019; Rasp, 2020; Bonavita and Laloyaux, 2020; Nguyen et al., 2021; Gottwald and Reich, 2021; Brajard et al., 2021). Both approaches imply an intervention on the original model: the first approach yields surrogate data-driven models of the full original system, while the second approach builds hybrid models with data-driven and physics-based components. In either case the spectrum of the LEs of these new models can be computed using the standard approach (Benettin et al., 1980b,a; Kuptsov and Parlitz, 2012), and can be compared to that of the original model as a way to quantify the goodness of the ML-reconstructed dynamics (Pathak et al., 2017; Brajard et al., 2020).

In contrast to these two families of methods, this study aims towards improving prediction skills by equipping the model with an external tool to quantify in real-time the local degree of predictability, and thus guide “non intrusive”

adaptations whereby the model equations are left unaltered. More specifically, the goal is to use ML to predict the LLE spectrum in an imminent time window given input of the system state at the current and (possibly) most recent time steps. We envisage that the trained ML algorithm could then be interrogated for information about the local dynamical instability whilst performing the numerical model forward integration. Such information could drive a decision process for adaptive modelling, for example adapting the numerical integration scheme to mitigate error, or adjusting the ensemble size when doing ensemble-based data assimilation or probabilistic predictions.

We test the ability of some popular supervised ML algorithms to perform this task in two prototypical low-dimensional chaotic dynamical systems. This study is concerned solely with the predictive capability of ML methods: the task of optimising the computational cost of making predictions is left for future work. We anticipate that the latter task will be largely dependent on the specific use-case and computing hardware. The ML algorithms we test are regression trees (RTs) (Breiman et al., 1984), multilayer perceptrons (MLPs) (e.g. see Goodfellow et al., 2016, Chapter 6), convolutional neural networks (CNNs) (LeCun et al., 1990), and long short-term memory networks (LSTMs) (Hochreiter and Schmidhuber, 1997; Graves, 2012). These algorithms encompass three approaches to exploiting the temporal structure of the input. We evaluate both their point-wise accuracy and their statistical performance, measured in this case by the closeness of the distribution of predictions to the distribution of the target values. We find that on average the machine learning algorithms predict the stable local Lyapunov exponent accurately, the unstable exponent reasonably accurately, and the neutral exponent only somewhat accurately. Each exponent is predicted more accurately in the Lorenz 63 system than in the Rössler system. We show that greater prediction accuracy is associated with local homogeneity of the local Lyapunov exponents on the system attractor. Importantly, the situations in which (forecast) errors grow fastest are not necessarily the same as those where it is more difficult to predict local Lyapunov exponents with machine learning.

The rest of this paper is organised as follows. In Section 2, we briefly review the theory of LEs and detail the method used to compute them. In Section 3 we pose and conceptualise the ML problem we intend to solve, motivate the choice of the algorithms, and detail the input and target data and the evaluation metrics. In Section 4 we present the two systems under consideration: the Rössler and the Lorenz 63 models and discuss the characteristics of their Lyapunov spectra. In Section 5 we present the results and Section 6 concludes with a discussion.

2 | LYAPUNOV EXPONENTS

2.1 | Overview of the theory

We review briefly the theory of LEs, with the aim of providing an intuitive explanation of what they are. The section follows Legras and Vautard (1996); Benettin et al. (1980b,a); Kuptsov and Parlitz (2012); Pikovsky and Politi (2016) and Strogatz (2018, Chapter 9, Section 3), to which we refer the reader for a more rigorous and comprehensive treatment.

Consider a deterministic autonomous dynamical system

$$\dot{\mathbf{x}} = \mathbf{g}(\mathbf{x}), \tag{1}$$

where $\mathbf{x} \in \mathbb{R}^n$ is the state of the system, $\mathbf{g}: \mathbb{R}^n \rightarrow \mathbb{R}^n$ is the evolution function, and $\dot{\mathbf{x}}$ denotes the derivative of \mathbf{x} with respect to time. To refer to a trajectory of the system that starts at an initial condition $\mathbf{x}(0) \in \mathbb{R}^n$, it is useful to define the flow function of the dynamical system in Equation 1 as $\mathbf{f}_{\mathbf{x}(0)}: \mathbb{R} \rightarrow \mathbb{R}^n$, where $\mathbf{f}_{\mathbf{x}(0)}(t)$ is the system state at time t , and the system state at time zero is $\mathbf{x}(0)$. A trajectory of the dynamical system starting at initial condition $\mathbf{x}(0)$ is the set $\{\mathbf{f}_{\mathbf{x}(0)}(t): t \in \mathbb{R}_{\geq 0}\}$.

Consider the distance between the trajectory started from the “true” initial condition $\mathbf{x}(0)$, and a trajectory started from the perturbed initial condition $\mathbf{x}(0) + \delta\mathbf{x}$. In particular, we are interested in the evolution of the perturbation vector \mathbf{v} , defined as

$$\mathbf{v}(t) = \mathbf{f}_{\mathbf{x}(0) + \delta\mathbf{x}}(t) - \mathbf{f}_{\mathbf{x}(0)}(t). \quad (2)$$

Note that this implies $\mathbf{v}(0) = \delta\mathbf{x}$. The idea behind LEs is to find $\lambda(t)$, where

$$e^{t\lambda(t)} = \frac{\|\mathbf{v}(t)\|}{\|\mathbf{v}(0)\|} \quad (3a)$$

$$\Leftrightarrow \lambda(t) = t^{-1} \ln \left(\frac{\|\mathbf{v}(t)\|}{\|\mathbf{v}(0)\|} \right). \quad (3b)$$

Namely, we seek the exponential growth rate of the initial error. In this setting, $\lambda(t)$ is specific to the initial condition $\mathbf{x}(0)$ and perturbation $\delta\mathbf{x}$, and $\lambda(t)$ varies with time.

Lyapunov exponents generalise this notion to describe a) average exponential growth rates of the system, regardless of the initial condition, b) the exponential growth rates for perturbations in all directions, and c) the exponential growth rates only for perturbations that are infinitesimally small. To measure the exponential growth rates in all directions, we consider perturbations contained in an n -sphere of infinitesimal radius. As time progresses, perturbations within the sphere are mapped into an ellipsoid. The LEs are the time-average of the exponential growth rate of the ratios between the axes of the sphere and of the ellipsoid (Legras and Vautard, 1996).

The theory starts by looking at the growth of a perturbation along a specific trajectory. Let us fix an initial condition $\mathbf{x}(0)$ and let \mathbf{v} be an infinitesimally small perturbation, as defined by Equation 2. Then the dynamics of the perturbation are given by

$$\dot{\mathbf{v}} = \mathbf{J}_{\mathbf{g}}\mathbf{v}, \quad (4)$$

where $\mathbf{J}_{\mathbf{g}}$ is the Jacobian of \mathbf{g} evaluated at $\mathbf{f}_{\mathbf{x}(0)}(t)$, *i.e.* the linearisation of the evolution function at $\mathbf{f}_{\mathbf{x}(0)}(t)$. We use the Jacobian since the systems considered here are assumed to be continuous and smooth, although Lyapunov exponents can be defined in a more general setting (*e.g.* see Pikovsky and Politi, 2016).

The solutions to Equation 4 can be found using a fundamental matrix, *i.e.* any matrix-valued function $\mathbf{M}(t)$ satisfying

$$\dot{\mathbf{M}} = \mathbf{J}_{\mathbf{g}}\mathbf{M}, \quad (5)$$

and such that $\mathbf{M}(t)$ is non-singular for all t . Given a fundamental matrix \mathbf{M} , any solution $\mathbf{v}(t)$ to Equation 4 can be written as

$$\mathbf{v}(t) = \mathbf{M}(t)\mathbf{c} \quad (6)$$

for some $\mathbf{c} \in \mathbb{R}^n$. We could set $\mathbf{M}(t)$ to be the leading order terms of the Magnus expansion $\exp(\Omega(t))$ for Equation 4 (see Iserles, 2011), but in practice we calculate $\mathbf{M}(t)$ by numerically integrating Equation 5. We are free to choose the initial value $\mathbf{M}(0)$ to be any non-singular matrix, since given one fundamental matrix $\mathbf{M}(t)$, and a non-singular matrix with constant coefficients \mathbf{P} , we can define a new fundamental matrix $\mathbf{A}(t) = \mathbf{M}(t)\mathbf{M}(0)^{-1}\mathbf{P}$ such that $\mathbf{A}(0) = \mathbf{P}$. The

solutions to Equation 4 are then given by $\mathbf{v}(t) = \mathbf{A}(t)\mathbf{c}'$, where $\mathbf{c}' = \mathbf{P}^{-1}\mathbf{M}(0)\mathbf{c}$. For simplicity, set $\mathbf{M}(0) = \mathbf{I}$, so that $\mathbf{c} = \mathbf{M}(0)^{-1}\mathbf{v}(0) = \mathbf{v}(0)$.

For the purpose of illustration we return to Equation 3a, from which it follows that

$$e^{\lambda(t)} = \left(\frac{\|\mathbf{v}(t)\|}{\|\mathbf{v}(0)\|} \right)^{\frac{1}{t}} = \left(\frac{\sqrt{\mathbf{v}(0)^{\top}\mathbf{M}(t)^{\top}\mathbf{M}(t)\mathbf{v}(0)}}}{\sqrt{\mathbf{v}(0)^{\top}\mathbf{v}(0)}}} \right)^{\frac{1}{t}}. \quad (7)$$

We are interested in the value of $\lambda(t)$ as $t \rightarrow \infty$.

$$\begin{aligned} \lambda(t) &= \lim_{t \rightarrow \infty} \ln \left[\left(\frac{\sqrt{\mathbf{v}(0)^{\top}\mathbf{M}(t)^{\top}\mathbf{M}(t)\mathbf{v}(0)}}}{\sqrt{\mathbf{v}(0)^{\top}\mathbf{v}(0)}}} \right)^{\frac{1}{t}} \right] \\ &= \lim_{t \rightarrow \infty} \ln \left[\left(\mathbf{v}(0)^{\top}\mathbf{M}(t)^{\top}\mathbf{M}(t)\mathbf{v}(0) \right)^{\frac{1}{2t}} \right]. \end{aligned} \quad (8)$$

This completes the illustration. However, the illustration is limited since the quantity $\lambda(t)$ in Equation 8 is the exponential growth rate for one perturbation only.

We consider now the full spectra of $\lambda_i(t)$, $i = 1, \dots, n$ that arise when one considers a sphere of perturbations. The growth of a sphere of perturbations depends only on $\mathbf{M}(t)^{\top}\mathbf{M}(t)$. Thus we consider the limit $\mathbf{W}(\mathbf{x}(0))$ defined by

$$\mathbf{W}(\mathbf{x}(0)) = \lim_{t \rightarrow \infty} \left[\mathbf{M}(t)^{\top}\mathbf{M}(t) \right]^{\frac{1}{2t}}. \quad (9)$$

By the multiplicative ergodic theorem (Oseledets, 1968; Ruelle, 1979) the limit exists and, as implied by $\mathbf{W}(\mathbf{x}(0))$, depends on the initial condition $\mathbf{x}(0)$. Importantly, we can make an eigendecomposition of $\mathbf{M}(t)^{\top}\mathbf{M}(t)$ in the limit, which gives

$$\mathbf{W}(\mathbf{x}(0)) = \mathbf{P}(\mathbf{x}(0))\mathbf{D}\mathbf{P}^{\top}(\mathbf{x}(0)) \quad (10)$$

where the eigenvector matrix $\mathbf{P}(\mathbf{x}(0))$ is orthonormal. The resulting matrix of eigenvalues \mathbf{D} is unique and depends neither on $\mathbf{x}(0)$ nor on the norm of the vector space containing the perturbations (Kuptsov and Parlitz, 2012). The LEs, $\lambda_1 \geq \lambda_2 \geq \dots \geq \lambda_n$, are the natural logarithm of the diagonal elements of \mathbf{D} .

We finish with some remarks on the significance of the LEs. A chaotic system is a system with at least one positive LE. The LEs, above defined in terms of the growth of axes of a sphere of perturbations, are linked to the growth of the volume of the n -parallelepiped defined by the principle axes of the resulting ellipsoid (see Wolf et al., 1985). In fact, the sum of the LEs is equal to the average divergence of the flow (see Pikovsky and Politi, 2016, Section 2.5.4). Thus, in dissipative systems, the sum of the LEs is negative. Finally, continuous chaotic systems have at least one LE equal to zero. This is due to there being zero growth of an infinitesimal perturbation in the direction of the flow.

2.2 | Computation of local and global Lyapunov exponents

The theory does not translate directly to a method for calculation of the LEs, since in order to approach the limit in Equation 9 one must integrate Equation 5 to find $\mathbf{M}(t)$ for very large t . This both accumulates numerical errors and results in a range eigenvalues of $\mathbf{M}^{\top}(t)\mathbf{M}(t)$ that is too large for accurate numerical calculation (Pikovsky and Politi,

2016). Instead, we measure the growth of n perturbations over (finitely) many small time intervals: to get the LLEs we calculate the natural logarithm of the ratios and divide by the length of the time interval, as shown in Equation 3b. If the system is ergodic, the arithmetic mean of the LLEs converges to the LEs as the number of time intervals increases.

Crucially, the perturbation vectors are orthogonalised and resized between each time interval. Orthogonalising the propagated perturbations is necessary to keep the perturbations distinct, since perturbations will tend to be attracted towards the direction of largest growth. The resizing is necessary to prevent perturbations becoming too small or large to be represented by floating-point numbers. We now present the algorithm used to calculate LEs and LLEs in this work, which is based on methods presented in Benettin et al. (1980b,a); Kuptsov and Parlitz (2012); see also Sandri (1996); Ramasubramanian and Sriram (2000); Pikovsky and Politi (2016).

1. Calculate and store a long trajectory $\{\mathbf{f}_{\mathbf{x}(0)}(t) : t \in [0, T_{\text{end}}]\}$. We discard an initial transient period to ensure the trajectory is in the attractor. One can alternatively calculate the trajectory at the same time as integrating Equation 5 in Step 3a. below, which avoids the need to store a long trajectory.
2. Initialise a matrix of perturbations $\mathbf{Q}_0 = [\mathbf{q}_0^1, \mathbf{q}_0^2, \dots, \mathbf{q}_0^n]$, such that the $\mathbf{q}_0^i \in \mathbb{R}^n$ are orthogonal and of unit length, that is, orthonormal. It is simpler computationally, although not necessary, to have unit-length perturbations.
3. Repeat the following iteration m times, where m is large enough to achieve convergence of the LEs. In iteration j , starting with $j = 1$, perturbations are propagated along the trajectory $\{\mathbf{f}_{\mathbf{x}(0)}(t) : t \in [(j-1)\tau, j\tau]\}$, where τ is a small positive real number. Each iteration results in n LLEs: λ_j^i , $i = 1, \dots, n$. Henceforth we notate LEs with hatted lambdas to distinguish the asymptotic LE $\hat{\lambda}_i$ from the unhatted LLE λ_j^i .
 - a. Calculate $\mathbf{M}(j\tau)$ by integrating Equation 5 with initial condition $\mathbf{M}((j-1)\tau) = \mathbf{I}$, where \mathbf{I} is the identity matrix.
 - b. Propagate the perturbations: $\mathbf{V}_j = \mathbf{M}(j\tau)\mathbf{Q}_{j-1}$, where \mathbf{Q}_{j-1} is from iteration $j-1$.
 - c. Orthonormalise the propagated perturbations \mathbf{V}_j to get \mathbf{Q}_j using QR-decomposition, (Golub and Van Loan, 2013; Strang, 2016)

$$\mathbf{Q}_j \mathbf{R}_j = \mathbf{V}_j, \quad (11)$$

where \mathbf{R}_j is upper triangular with positive elements on the diagonal.

- d. The i^{th} diagonal element r_j^i of \mathbf{R}_j is the norm of the orthogonalised (but not normalised) \mathbf{v}_j^i , here denoted $\tilde{\mathbf{v}}_j^i$. Since the columns \mathbf{q}_{j-1} of \mathbf{Q}_{j-1} are normalised, the diagonal elements are the ratios we need: $r_j^i = \|\tilde{\mathbf{v}}_j^i\| / \|\mathbf{q}_{j-1}^i\|$. The n LLEs at time $(j-1)\tau$, the start of iteration j , are calculated as

$$\lambda_j^i = \tau^{-1} \ln(r_j^{\alpha(i)}). \quad (12)$$

In Equation 12 the diagonal element $r_j^{\alpha(i)}$ is indexed by labelling function $\alpha(i)$, where $\alpha(i)$ is determined (in Step 4) so that the LE computed from the LLEs $\{\lambda_j^i \mid j = k, \dots, m\}$ is the i^{th} largest LE. This is necessary since the mean of the LLEs computed from r_j^i does not necessarily converge to the i^{th} -largest LE.

4. Calculate the LEs:

$$\hat{\lambda}_i = (m-k)^{-1} \sum_{j=k+1}^m \lambda_j^i \quad i = 1, \dots, n \quad (13)$$

where the LLEs from the first k iterations are discarded. The bijective function α takes inputs and values $1, \dots, n$, and is chosen such that the global LEs are numbered in descending order, *i.e.* such that $\hat{\lambda}_i \geq \hat{\lambda}_{i+1}$. In the case that

there is a degeneracy, *i.e.* two or more LEs have the same value, there will be multiple possible labelling functions α . We say i^{th} LLE to refer to any set of LLEs $\{\lambda_j^i: j = k, \dots, m\}$ that are associated to the i^{th} LE.

In Step 4, a transient period of length k iterations is required to let the initial perturbations \mathbf{Q}_0 converge to the dynamics of the trajectory so that the leading perturbation \mathbf{q}_j^1 is oriented in the direction of largest growth. The LLE is theoretically defined in terms of an n -sphere of infinitesimal perturbations and the ellipsoid that results from applying the tangent linear propagator \mathbf{M} to the n -sphere. In particular, the LLEs are defined in terms of ratios of the axes of the n -sphere and the ellipsoid. In practice, given an initial set of perturbations \mathbf{Q}_0 , it is unlikely that the leading perturbation \mathbf{q}_0^1 will be mapped by $\mathbf{M}(\tau)$ onto the leading axis of the ellipsoid, which will lead to a poor estimation of the LLE. However, with sufficiently many iterations k , \mathbf{q}_k^1 will be attracted to the direction of largest growth, which will lead to more accurate estimates of the LLE.

The algorithm for computing the LLEs and LEs does not scale well. The computational cost of the steps of the algorithm are as follows. The length of the required transient period, *i.e.* the number of "spin-up" iterations, depends on the system dynamics and, in the worst case, grows proportionally to the system dimension n (Kuptsov and Parlitz, 2012, p. 754). For computing LEs, the total number of iterations m depends on the complexity of the attractor and the precision required. Each iteration (Step 3) requires the calculation of a trajectory of length τ , which involves at least $O(n)$ floating point operations (flops). The cost of integrating the matrix differential Equation 5 involves at least one evaluation of the Jacobian matrix, and at least one multiplication of the Jacobian by another matrix, per timestep. For a dense, non-trivial Jacobian, it is reasonable to assume that Step a. involves $O(n^2)$ flops in the simplest case, namely where $\tau = \Delta t$ and a minimal numerical integration scheme is used. In a less simple case, Step a. will require at least $O(n^{2.3})$ flops: the cost of multiplying two dense $n \times n$ matrices (Alman and Williams, 2021). Step b. also involves multiplying two (possibly dense) $n \times n$ matrices. Step c. is by far the most expensive step, since computing eigenvectors and eigenvalues via QR decomposition requires $25n^3$ flops (Golub and Van Loan, 2013; Arbenz, 2016). The overall theoretical time complexity of the LE algorithm is thus $25n^3 + O(n^2)$ flops. In practice, $n \times n$ matrix multiplication can be much slower (at least $O(n^3)$) due to memory access latency (Albrecht et al., 2010). Consequently, computing the full LLE spectrum for a modern weather prediction system (where $n \approx 10^9$) is too expensive to be done during the forecast cycle.

3 | USING SUPERVISED MACHINE LEARNING TO ESTIMATE LYAPUNOV EXPONENTS

3.1 | Problem statement and evaluation metrics

Supervised learning refers to ML algorithms that use data sets formed of input-target pairs, whereby the goal is to construct a statistical model that emulates the idealised function that maps from the input to the target. The input and target are multidimensional arrays of data, not necessarily of the same dimensions. A single input-target pair is known as an example; the size of a ML data set refers to the number of examples it contains.

Supervised learning algorithms construct statistical models by optimising the model's parameters using the data. In the problem of this study, the input is the system state at a set of consecutive recent time steps including the current time t . The target is the vector of n LLEs calculated using the method described in Section 2.2 by integrating perturbations from the current time t to $t + \tau$. Generally, we have

$$(\text{input}, \text{target}) = \left((\mathbf{x}_{k-r}, \dots, \mathbf{x}_{k-1}, \mathbf{x}_k), (\lambda_k^1, \dots, \lambda_k^n) \right), \quad (14)$$

where we recall that $\mathbf{x}_k \in \mathbb{R}^n$ denotes the system state at time $k\Delta t$, and λ_k^i is the i^{th} LLE computed from the interval $[k\Delta t, k\Delta t + \tau]$.

Point-wise accuracy

By point-wise accuracy we refer to the ability of a ML algorithm to predict a specific LLE at an arbitrary time t . For its evaluation we calculate a separate R^2 score for each LLE in the spectrum, from a set of d predictions and targets. The R^2 score, also known as the coefficient of determination, is given by

$$R^2\left(\{(y_j, \hat{y}_j) \mid j = 1, \dots, d\}\right) = 1 - \frac{\sum_{j=1}^d (y_j - \hat{y}_j)^2}{\sum_{j=1}^d (y_j - \bar{y})^2} \in (-\infty, 1], \quad (15)$$

where, for each j , $y_j \in \mathbb{R}$ is the target output (e.g. the i^{th} LLE), $\hat{y}_j \in \mathbb{R}$ is the model's prediction, and \bar{y} is mean of the target outputs. In Equation 15, the numerator is known as the sum of squares of residuals, and the denominator is known as the total sum of squares. An R^2 score of 1 is optimal, and an R^2 score of 0 is as good as guessing the mean of the target values every time.

Similarity of prediction and target distributions

In addition to the point-wise accuracy, we evaluate the statistical accuracy of the ML models with quantile-quantile (QQ) plots. QQ plots provide a simple non-parametric tool to compare the empirical probability distributions generated by two samples (Wilk and Gnanadesikan, 1968). In our case these are the predicted and the target values. To generate the plot, a set of quantiles (the 1000-quantiles in our experiments) is computed for both samples. These quantiles are then plotted against each other in a scatter plot. If the two samples have the same empirical distributions, the scatter plot renders a 45 degree diagonal line (of course this is subject to sampling error, which diminishes as the sample size grows). Departures from this ideal result show differences in the location and scale parameters of the empirical distributions, as well as possible linear and non-linear relationships between the variables, see e.g. National Institute of Standards and Technology (U.S.) (2012) for a more detailed discussion. In our case, the QQ plots are useful to show which parts of the target distribution are well represented by the predictions.

3.2 | Supervised learning algorithms

We test four supervised learning algorithms, summarised in Table 1, all well known in the ML community. They are prototypical of three distinct approaches to using temporal structure when learning patterns from the data (two methods make use of the same approach as clarified later). Here by temporal structure we mean the temporal sequence of elements in each input vector, as opposed to the pairwise relation between the inputs and outputs while segmenting the time-series for data set preparation. The relative success of each algorithm gives insight into the nature of the problem from the ML perspective.

The first approach to learning from the data is to treat each element of the input vector (each feature) as an independent and identically distributed variable. We test two algorithms that take this approach: a multilayer perceptron (MLP) (as described in e.g. Goodfellow et al., 2016, Chapter 6) and a regression tree (RT) (Breiman et al., 1984). Both algorithms have no inherent preference with respect to the temporal structure of the data, since they are invariant to the choice of order of the input features (a choice which is made in the preprocessing stage before training the algorithm). In fact, the RT may make use of only a few features from the set available in the input vector (Breiman

Algorithm	Architecture
Multilayer perceptron (MLP)	One or more dense layers and one dense output layer
Regression tree (RT)	One tree per target LLE
Convolutional neural network (CNN)	One 1D-convolution layer, max pooling layer, flatten layer, one or more dense layers
Long-short term memory network (LSTM)	One or more LSTM layers, one dense output layer

TABLE 1 The four supervised learning algorithms used in this study. The hyperparameter values (e.g. number of dense layers) used in the experiment are described in Section 5.2

et al., 1984).

An MLP is a basic feedforward artificial neural network (NN). In our experiments, each layer in the MLP is densely connected with the previous layer. The RT is the only non-NN algorithm we test; RTs function by evaluating a finite chain of comparisons on the input features, such as “ $x_k > 0$ ”. The chain of comparisons form a tree graph; each leaf node corresponds to an output value. Thus RTs have finitely many possible output values. The key advantage of a RT is its low computational cost of making predictions. Other advantages include the implicit feature selection process and potentially greater explainability of predictions compared with NNs. By setting two hyperparameters (the maximum number of leaf nodes and the maximum depth, *i.e.* number of consecutive comparisons before a leaf node), it is possible to greatly constrain the size of the resulting tree. For simplicity, we opt to train a separate RT for each target LLE: *i.e.*, the prediction of the target vector $(\lambda_k^1, \dots, \lambda_k^n)$ is made by n RTs, where each RT predicts a different λ_k^i .

The second approach to learning from the data attempts to exploit the temporal structure by only being sensitive to patterns that appear in small time windows within the input. This is the approach taken by the third algorithm, a convolutional neural network (CNN) (LeCun et al., 1990) that uses convolution to exploit such patterns. In our experiments, the CNN is comprised of one 1D-convolution layer with a kernel of size two, a max-pooling layer (if the number of time steps in the input is greater than 2), a flattening layer and finally a set of dense layers (the number of which is optimised as described in Section 5.2). The “1D” aspect of the 1D-convolution layer is that the layer convolves over the time dimension. The kernel size of two means that if the input is comprised of system state vectors at $r + 1$ consecutive time steps, the convolution layer is only sensitive to patterns that may occur in any time window of length two within the $r + 1$ time steps. The max-pooling layer has a pool size and stride of two, which results in an invariance to translation of patterns by a single time step.

The third approach attempts to exploit the temporal structure by being sensitive to the sequential order of the input features in time. This is the approach taken by the long short-term memory network (LSTM) (Hochreiter and Schmidhuber, 1997; Graves, 2012). An LSTM is a form of recurrent neural network (RNN), where the flow of information in and out of the NN’s hidden state is controlled by learned gates. LSTMs have been successful in various tasks where there are long term dependencies, *i.e.* where the correct output at a later element in the sequence requires information from elements further back in the sequence. Such tasks include speech recognition (Graves et al., 2013) and machine translation (Wu et al., 2016). In machine translation, for instance, it is useful to retain information about words early on in the sentence to best predict how to translate words at the end of the sentence. In the experiments of this study, the LSTM layers process the input one time step at a time, in chronological order. The estimation of the LLEs is made after the last time step has been processed.

All NN-like algorithms (MLP, CNN and LSTM) were implemented using Tensorflow (Abadi et al., 2015). Additionally, all NN algorithms standardise the input and target data by subtracting the mean and dividing by the standard deviation, where the mean and standard deviation are calculated from the training set. Each component of the input

and target is standardised independently. This is to make the data more amenable to learning. The scaling pipeline was implemented using Scikit-learn (Pedregosa et al., 2011). For the RT, we use the implementation in the Scikit-learn Python module (Pedregosa et al., 2011).

4 | RÖSSLER, LORENZ 63 AND THEIR LOCAL LYAPUNOV SPECTRA

In this section we present the two dynamical systems used in this work. We discuss the characteristics of their attractors and their LLEs, as this forms the data for the ML models and will be important in understanding their performance. The Rössler (Rössler, 1976) and the Lorenz 63 (Lorenz, 1963) systems are both three-dimensional, continuous time, ODE dynamical systems, given respectively by Equations 16 and 17:

$$\begin{aligned}
 \text{Rössler} \quad & \begin{aligned} \dot{x} &= -y - z \\ \dot{y} &= x + ay \\ \dot{z} &= b - z(x - c) \end{aligned} & (16)
 \end{aligned}$$

$$\begin{aligned}
 \text{Lorenz 63} \quad & \begin{aligned} \dot{x} &= \sigma(y - x) \\ \dot{y} &= x(\rho - z) - y \\ \dot{z} &= xy - \beta z \end{aligned} & (17)
 \end{aligned}$$

It is easy to compute the analytic Jacobian matrices from these equations. Furthermore, the small size of both systems allow us to perform exhaustive experiments with long time series. We use the parameters $(a, b, c) = (0.37, 0.2, 5.7)$ and $(\sigma, \rho, \beta) = (10, 28, 8/3)$. These are commonly chosen values for which the systems exhibit chaotic behaviour (see e.g. Ott, 2002). Under these settings, both systems are dissipative, and they possess strange attractors of fractal dimension.

The data used in our results are generated following Section 2.2. The evolution equations, Equations 16 and 17, as well as the corresponding fundamental matrix equation, Equation 5, are integrated using a fourth-order Runge-Kutta scheme with timestep $\Delta t = 0.01$ for both systems. The LLEs are calculated over time windows of length $\tau = 0.04$ (*i.e.* four timesteps); the LLEs at time t are calculated by integrating perturbations from time t to $t + \tau$. We choose $\tau = 0.4$, rather than a smaller value, so that the resulting set of LLEs provide a better coverage of the attractor. Table 2 shows the resulting LLEs.

System	$\hat{\lambda}_1$	$\hat{\lambda}_2$	$\hat{\lambda}_3$
Rössler	0.19597 ± 0.00011	0.0000075 ± 0.0001275	-4.30097 ± 0.00068
Lorenz 63	0.90495 ± 0.000145	0.001975 ± 0.000055	-14.571345 ± 0.000105

TABLE 2 The LLEs of the Rössler and Lorenz 63 systems as calculated following Section 2. These values are computed from 718,800 LLE iterations, following a transient of $k = 1, 200$ iterations. As described in Section 2, the arithmetic mean of the LLEs converges to the LLEs as one includes LLEs from more iterations, *i.e.*, from a longer trajectory. The convergence is not monotonic: the series of arithmetic means fluctuates as the number of LLEs increases. To give an indication of the precision of the numerical calculation, we therefore calculate the LLE as the mid-point of the range of the series of arithmetic means acquired from the first j LLEs, where $j = 716, 801, \dots, 718, 800$. The extent of the range above and below this value are also given. The proximity of the second LLE to zero is a test for the accuracy of the numerical algorithm, since the middle LLE is theoretically known to be zero in chaotic autonomous continuous-time systems (Pikovsky and Politi, 2016).

In Figures 1 and 2, the top row shows the values of the LLEs along the systems' trajectories, specifically for the

points $\mathbf{f}_{\mathbf{x}(0)}(\tau_j)$ where $1,200 \leq j \leq 26,199$; the values of the LLEs are given in color. We show only 25,000 data points to avoid saturating the figures: the local heterogeneity of the LLE values in phase space is evident. The bottom row displays the distribution of LLE values via histograms, for the points $\mathbf{f}_{\mathbf{x}(0)}(\tau_j)$ where $1,200 \leq j \leq 719,999$. The i th column shows the LLEs associated with the i th LE.

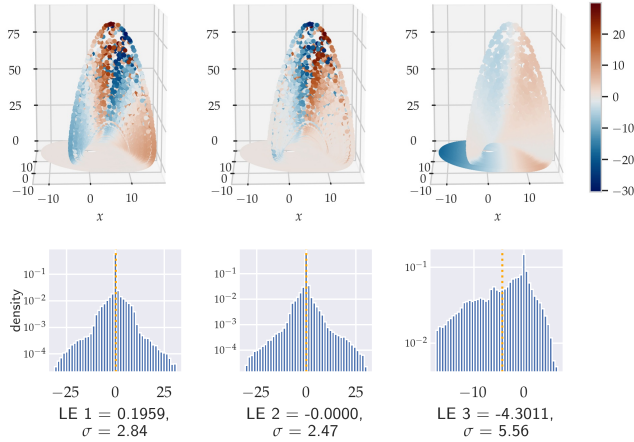


FIGURE 1 A long-time trajectory of the Rössler system coloured by LLE values (top row) shows how LLE values tend to be arranged in the system's attractor. The bottom row shows the corresponding statistical distribution of the LLEs via histograms; the mean of the LLE values is shown by the dotted orange line. The top panels show the same collection of 25,000 points. On the other hand, the histograms are generated from the full set of 718,800 LLEs; note that the vertical axis is plotted in logarithmic scale. The mean (i.e. the corresponding LE) and standard deviation of the LLE values in each column are shown underneath.

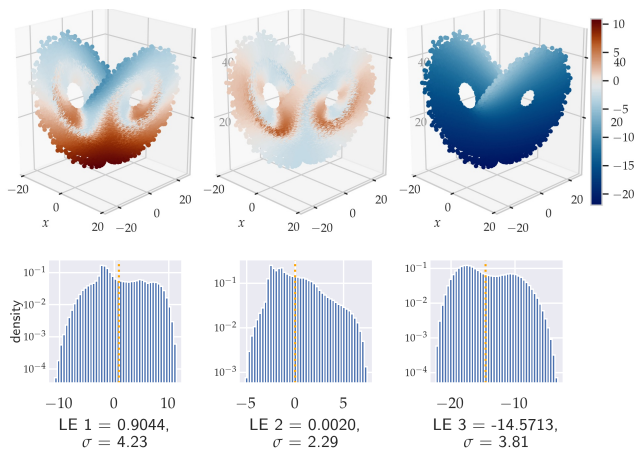


FIGURE 2 As with Figure 1 but for Lorenz 63.

Let us first consider the statistical distribution of the LLEs. In the Rössler system (Figure 1) there is a marked

difference between the first two LLE distributions and the third. The first two have a single, tall, thin mode with long tails and are roughly symmetric. The distribution of the third LLE has a lower-density mode with thicker tails and is negatively skewed. The range of values of the third distribution is also much smaller than that of the first two.

The Lorenz 63 system LLE distributions differ from those of the Rössler system. All three LLE distributions (Figure 2) have thicker tails and are positively skewed. The first and third are weakly bimodal, whilst the second is unimodal.

We now introduce a property that will be important to understanding the performance of the ML. In the context of the distribution of LLEs in the attractor of a system, we say that a region U of the attractor A is (*locally*) *heterogeneous* if the function $f: A \rightarrow \mathbb{R}$ mapping from A to the i th LLE value is non-smooth in U . The best definition in more simple terms is that the LLE values in U vary in a non-smooth fashion across U . For example, an alternating lattice (such as a chess board) would be locally heterogeneous. If U is not heterogeneous, we say it is homogeneous. In this work we use homogeneous and heterogeneous only in the sense of *locally across a small region of phase space U* , and not in the sense of across the entire attractor (*i.e.* globally), or along a trajectory (*i.e.* across time), as is the case in, *e.g.*, Vannitsem (2017), and Lucarini and Gritsun (2020).

For all three Rössler LLEs, in the disc of the attractor that sits in the xy -plane, the LLE values are homogeneous. In the loop that jumps out of the disc with positive z -values, there are bands of similar values for all three LLEs. For the first two LLEs, the most extreme LLE values are in the loop, and there is significant local heterogeneity within the bands. For example, there are some small regions of the attractor where the first LLE is 10 or above for the majority of points, yet for some other points it is as low as -20 . This high degree of heterogeneity is reflected in the longer tails of the distributions of the first and second LLEs (*cf* Figures 1 and 2). In contrast, the third LLE is locally homogeneous: the colour change in the graph is smooth.

Note that the trajectory of the Rössler system spends more time in the disc than in the loop. Consequently, data points in the loop are considerably sparser.

In the Lorenz 63 system, the first two LLEs have distinct regions of local heterogeneity and homogeneity. Unlike with the Rössler system, the regions of greater mixing are along the boundaries between regions of greater local homogeneity. The most extreme values of the first LLE are at the bottom of the attractor (z close to 0) and on the top edge of the wings: not in the regions of local heterogeneity. The third LLE, as with the Rössler system, is everywhere locally homogeneous.

As we will see, the characteristics of the LLEs we have discussed have implications for the performance of the ML methods trying to estimate them.

5 | EXPERIMENTS AND RESULTS

5.1 | Experiment setup

Having described the ML algorithms (Section 3.2) and dynamical systems (Section 4) used in this work, this section details the experiments and results. The experiments test a total of 16 configurations, which consist of each combination of two dynamical systems, four ML algorithms, and two input types:

$$\begin{aligned} \text{Input Type 1:} & \quad (\mathbf{x}_k) \\ \text{Input Type 2:} & \quad (\mathbf{x}_{k-5}, \mathbf{x}_{k-4}, \mathbf{x}_{k-3}, \mathbf{x}_{k-2}, \mathbf{x}_{k-1}, \mathbf{x}_k) \end{aligned} \tag{18}$$

The first input type consists of the current time step only, whereas the second has the current time step and the five preceding time steps. Note that if there is only one time step in the input, the CNN is equivalent to an MLP where the number of units in the first hidden layer of the MLP is twice the number of filters in the CNN.

For each dynamical system, we created a data set of 100,000 examples using the method described in Section 2.2, and the parameters given in Section 4. From each system's data set we generate 30 data set instances, where each instance is a unique random shuffle of the 100,000 examples. Each data set instance is partitioned into training, validation and test sets with a ratio of 0.6 : 0.2 : 0.2. The training, validation and test sets of different data set instances are therefore distinct. Given that the Rössler system and Lorenz 63 system are both ergodic, and the size of the training, validation and test data sets are large, the coverage of the attractors by examples in each data set instance is similar to that which would be achieved if we had instead generated 30 sets of new data. Each configuration is tested on the 30 data set instances, *i.e.* each configuration is tested in 30 trials. This provides an estimate of the variability of performance of each algorithm.

The NNs (MLP, CNN, LSTM) are implemented with two methods for preventing overfitting: activity regularisation on each layer, and early stopping. Regularisation penalises large weight values; early stopping selects the model weights that score optimally on the validation data set, rather than on the training data set.

5.2 | Hyperparameter optimisation

In ML, *hyperparameter* refers to any parameter that has to do with the form of, or method of optimising, the statistical model, as opposed to the trainable parameters of the model itself (often referred to as weights). Hyperparameters are fixed before the model is fit to the data, *i.e.* before the weights are optimised. For example, one hyperparameter for a NN is the learning rate: the amount by which model weights are changed at each step in the optimisation. Selecting the right hyperparameters is essential for effective use of ML algorithms (Goodfellow et al., 2016).

We use a Bayesian optimisation method, implemented by Scikit-Optimize (Head et al., 2021), to optimise the hyperparameters for each ML algorithm used in this study. Conceptually, a Bayesian optimisation method is an informed hyperparameter search that generates a probabilistic model (*e.g.*, using a surrogate Gaussian process regression) of the true ML model (*e.g.*, CNN) to select a set of hyperparameters that maximises the true ML model's performance (Snoek et al., 2012).

We perform separate hyperparameter optimisation for each configuration. Hyperparameter optimisation was carried out on Google's tensor processing units (TPUs) using Google Colaboratory. The search domain for each hyperparameter was chosen based on users' knowledge of the algorithms, the nature of the problem, and common practice in the ML community (Hastie et al., 2009; Goodfellow et al., 2016). The search domains are shown in Table 3. The chosen search space permits the NNs to be reasonably large (up to 200 neurons per layer and up to 10 layers) given the low-dimensionality of the task: mapping from three (3 variables \times 1 time steps), or eighteen (3 \times 6) features to three outputs. On the other hand, we opted to restrict the maximum number of layers for the LSTM due to the greater complexity of the algorithm. In fact, the first attempt to perform hyperparameter optimisation with a 6-layer LSTM exceeded the 24 hours runtime limit for Google Colaboratory. In contrast to the NNs, we forced the RTs to remain computationally light by limiting *maximum leaf nodes* (*i.e.* the maximum number of possible output values) to 100. The entire hyperparameter optimisation process had a combined runtime of 108 hours. Although the hyperparameter optimisation was computationally expensive it was affordable in the low dimensional problems at hand. It greatly increases the chance that we attain maximal performance from each ML algorithm, thus providing useful insights into the problem from a ML perspective.

The optimised hyperparameter values, resulting from 50 iterations of the optimisation algorithm, are presented

Algo	Hyperparameter	Search domain
RT	maximum depth	[1, 100]
	maximum leaf nodes	[5, 100]
	maximum features	{auto, \log_2 , square root, none}
	splitter	{best, random}
	min. cost-complexity pruning parameter	$[1 \times 10^{-6}, 100]$
	minimum examples per leaf	[1, 20]
	minimum weight fraction per leaf	{0, 0.5}
MLP	learning rate	$[1 \times 10^{-6}, 0.9]$
	number of layers	[1, 10]
	number of neurons per layer	[1, 200]
	activity regularisation on each layer	{L1($\alpha = 0.001$), L2($\alpha = 0.001$), None}
CNN	learning rate	$[1 \times 10^{-6}, 0.9]$
	number of filters	[1, 100]
	number of dense layers	[1, 10]
	number of neurons per dense layer	[10, 200]
	activity regularisation on each layer	{L1($\alpha = 0.001$), L2($\alpha = 0.001$), None}
LSTM	learning rate	$[1 \times 10^{-6}, 0.9]$
	number of LSTM layers	[1, 3]
	number of LSTM units per layer	[1, 200]
	activity regularisation on each layer	{L1($\alpha = 0.001$), L2($\alpha = 0.001$), None}

TABLE 3 The search domain for hyperparameters of the ML algorithms. For the MLP, CNN and the LSTM, the number of (dense) layers excludes the final densely-connected output layer with three units.

in Table 4. Some optimal values are at the boundary of the search domain (Table 3). This suggests that the algorithms might have performed better with hyperparameter values beyond the chosen search domain. For instance, in every experiment configuration, the optimised value of the RT hyperparameter *maximum leaf nodes* is 100, the maximum value in the search domain. Other examples of hyperparameters whose optimised values are at the boundary of the search domain for some configurations are the number of neurons per layer for the MLP and the CNN, and the number of LSTM units per layer. Nevertheless, the number of dense layers in the MLP and the CNN, as well as the number of LSTM layers, are mostly not at the boundary. Overall, from the results of the hyperparameter optimisation, we can argue that although greater prediction accuracy might be achieved using NNs with larger layers (more neurons or LSTM units), the number of layers (NN depth) in the experiments is adequate.

To give an idea of the complexity of each of the four optimised ML algorithms, Table 5 shows the size of the ML models, measured by the maximum number of comparisons for the RT and the number of trainable parameters in the case of the NNs. The model size is a function of the optimised hyperparameter values. For the NNs with 6 time steps as input, the model size of those that predict the Lorenz 63 system LLEs is larger than those that predict the Rössler system. This is perhaps reflective of the more chaotic dynamics of the Lorenz 63 system, which has a larger first LE as well as two non-linear terms in the equations as opposed to only one in the Rössler system (see Equations 16 and 17).

			Optimised value:			
			Rössler		Lorenz 63	
Algo	Target LLEs	Hyperparameter	1 time step	6 time steps	1 time step	6 time steps
RT	LLE 1	maximum depth	78	58	100	100
		maximum leaf nodes	100	100	100	100
		maximum features	auto	auto	auto	None
		splitter	best	random	best	best
		min. cost-complexity pruning parameter	1.641e-06	7.594e-05	1.000e-06	2.845e-06
		minimum examples per leaf	20	13	15	16
		minimum weight fraction per leaf	0	0	0	0
	LLE 2	maximum depth	100	24	100	78
		maximum leaf nodes	100	100	100	100
		maximum features	auto	auto	auto	None
		splitter	best	random	best	best
		min. cost-complexity pruning parameter	1.000e-06	1.000e-06	5.812e-04	4.616e-04
		minimum examples per leaf	20	20	1	1
		minimum weight fraction per leaf	0	0	0	0
	LLE 3	maximum depth	17	48	100	72
		maximum leaf nodes	100	100	100	100
		maximum features	auto	None	sqrt	auto
		splitter	best	best	best	best
min. cost-complexity pruning parameter		1.141e-04	2.739e-06	1.000e-06	2.052e-06	
minimum examples per leaf		2	1	14	20	
minimum weight fraction per leaf		0	0	0	0	
MLP	all	learning rate	7.300e-05	1.222e-04	7.628e-05	1.939e-05
		number of layers	7	6	8	10
		number of neurons per layer	200	182	165	200
		activity regularisation on each layer	L2	L2	L2	L1
CNN	all	learning rate	1.081e-04	1.586e-04	3.287e-04	1.016e-04
		number of filters	100	37	29	59
		number of dense layers	6	6	3	6
		number of neurons per dense layer	200	200	122	200
		activity regularisation on each layer	None	L1	L1	L1
LSTM	all	learning rate	2.857e-03	1.874e-03	2.722e-03	1.105e-04
		number of LSTM layers	3	1	2	2
		number of LSTM units per layer	62	100	100	100
		activity regularisation on each layer	L1	L1	L1	None

TABLE 4 The optimal hyperparameter values selected by 50 iterations of Bayesian optimisation.

The same is not true of the NNs that take 1 time step as input. This is unsurprising since the 1 time step input contains less information on the dynamics, *i.e.*, how the state variables are changing in time. In this case, the size of the MLP and the CNN is smaller in the Lorenz 63 system, whereas the size of the LSTM is larger in the Lorenz 63 system. Due to their architectural similarity in the 1 time step case, it is unsurprising that the optimal model size for MLP and CNN behaves similarly.

Algo		Rössler		Lorenz 63	
		1 time step	6 time steps	1 time step	6 time steps
RT	maximum comparisons	99	99	99	99
MLP	trainable parameters	242,603	170,537	192,888	366,203
CNN	trainable parameters	222,503	224,262	34,244	237,616
LSTM	trainable parameters	78,557	41,903	122,303	122,303

TABLE 5 The size of the ML models, measured by the number of comparisons (RT) and number of trainable parameters (NNs). The maximum number of comparisons for each RT is 99 (one less than the maximum leaf nodes), since the max depth is too large to constrain the number of non-leaf nodes in the tree.

The maximum size of the RTs is the same for all configurations. This is due to the tight restriction placed on the tree size by the search domain of the maximum leaf nodes hyperparameter (Table 3). However, the maximum depth hyperparameter varies across configurations and between LLEs. The optimal value of the maximum depth depends on the number of linear separations of the input space that improves the predictions during the generation of the tree from the training data. For the same input type, and for a given LLE, the RT for the Lorenz 63 system has a greater maximum depth than the RT for the Rössler system. The greater maximum depth implies that more accurate predictions can be made by separating the input space at smaller scales (*i.e.* making finer-grained partitions of the input space) in the Lorenz 63 system, compared to the Rössler system. In other words, there is clearer detail at smaller relative scales (in the input space) in the Lorenz 63 system than in the Rössler system.

5.3 | Results

Comparisons between systems and across the LLE spectrum

How accurately can the LLEs be predicted? We assess accuracy with the R^2 score of predictions made on the test data sets, each of which has 20,000 examples (see Table 6). There are 30 R^2 scores for each configuration: one from each data set instance. These R^2 scores are shown in boxplots in Figure 3 and summarised by their mean and standard deviation in Table 7. The immediate observation is that the R^2 scores differ consistently among LLEs (for a given system) and between systems (for a given LLE). The third LLE is well predicted in both systems, by all ML algorithms, and with both types of input. Apart from one case, the mean R^2 scores for LLE 3 are above 0.98. This is unsurprising given the local homogeneity of LLE 3 on the attractors, as discussed in Section 4. In all cases, the second LLE is the least well predicted (0.39 for Rössler system and 0.76 for Lorenz 63 system). This result is to be expected since it is known that the second LLE is calculated least accurately by the numerical method (Kuptsov and Parlitz, 2012) and has a slower convergence (Bocquet et al., 2017). The first LLE is predicted at least reasonably well in both dynamical systems (0.54 for Rössler system and 0.93 for Lorenz 63 system).

Next we compare prediction accuracy between dynamical systems. For LLEs 1 and 2, predictions of the Lorenz

Number of data set instances	30
Number of examples in each data set instance	100,000
Number of examples in the training partition	60,000
Number of examples in the validation partition	20,000
Number of examples in the test partition	20,000

TABLE 6 A summary of key values in the data setup. Note that each data set instance contains the same examples in a unique, shuffled order.

63 system tend to be better than those of the Rössler system. The highest mean R^2 score for LLE 1 is 0.9304 for the Lorenz 63 system, yet only 0.5365 for the Rössler system. For LLE 2 the highest mean R^2 score is 0.7613 for the Lorenz 63 system, yet only 0.3897 for the Rössler system. For LLE 3, the mean R^2 scores are similarly high in both systems. As we have described, these results indicate that the LLEs can be predicted and the variability of the prediction accuracy depends on which LLE and which dynamical system is being predicted.

R^2 scores of test data sets for all 30 data set instances

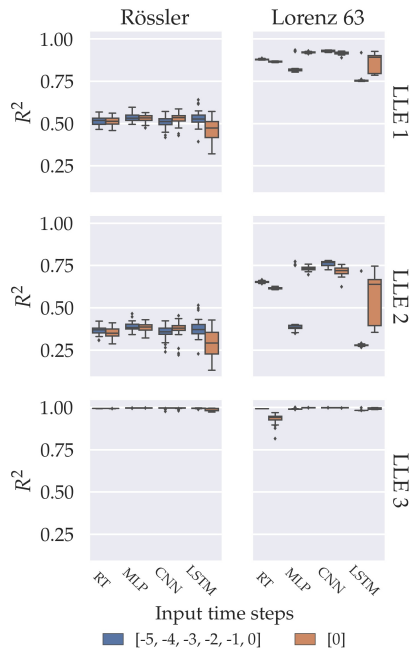


FIGURE 3 The R^2 scores of test data sets from the 30 trials, showing the variation across data set instances, for each combination of system and ML method. Perfect predictions have an R^2 score of one. Each test data set has 20,000 examples.

R^2 on test data: Mean and (standard deviation) of 30 data set instances						
Rössler	LLE 1		LLE 2		LLE 3	
	1 time step	6 time steps	1 time step	6 time steps	1 time step	6 time steps
RT	0.5155 (0.0248)	0.5161 (0.0268)	0.3506 (0.0299)	0.3681 (0.0278)	0.9944 (0.0002)	0.9946 (0.0002)
MLP	0.5323 (0.0211)	0.5363 (0.0243)	0.3837 (0.0249)	0.3897 (0.0274)	0.9978 (0.0005)	0.9975 (0.0006)
CNN	0.5279 (0.0333)	0.5054 (0.0349)	0.3711 (0.0518)	0.3530 (0.0419)	0.9960 (0.0040)	0.9956 (0.0044)
LSTM	0.4657 (0.0633)	0.5319 (0.0462)	0.2921 (0.0769)	0.3788 (0.0571)	0.9869 (0.0074)	0.9955 (0.0023)
Lorenz 63	LLE 1		LLE 2		LLE 3	
	1 time step	6 time steps	1 time step	6 time steps	1 time step	6 time steps
RT	0.8672 (0.0025)	0.8801 (0.0027)	0.6166 (0.0046)	0.6540 (0.0053)	0.9324 (0.0305)	0.9936 (0.0003)
MLP	0.9217 (0.0038)	0.8350 (0.0438)	0.7325 (0.0123)	0.4449 (0.1446)	0.9993 (0.0003)	0.9925 (0.0033)
CNN	0.9169 (0.0081)	0.9304 (0.0047)	0.7153 (0.0261)	0.7613 (0.0159)	0.9992 (0.0005)	0.9993 (0.0002)
LSTM	0.8659 (0.0530)	0.7594 (0.0302)	0.5702 (0.1419)	0.2933 (0.0803)	0.9955 (0.0044)	0.9838 (0.0028)

TABLE 7 The R^2 score measures the accuracy of predictions: the optimum score is 1. We calculate the R^2 on the test data set for each of the 30 trials. The table shows mean R^2 over 30 trials, and the corresponding standard deviations in parentheses. The highest mean R^2 score for each combination of LLE and system (for both input types) is shown in bold. “1 (6) time step(s)” refers to the number of time steps in the input.

Analysis of predictions on ordered test data

Figures 4 and 5 show time series of target values and predictions for a small set of ordered test data. The predictions are produced by the algorithm that results in the best R^2 scores for each system. The MLP achieves the highest mean R^2 score for the Rössler system, whilst the CNN achieves the highest for the Lorenz 63 system. In both systems, LLE 3 is almost perfectly predicted throughout the time series. However, the predictions of LLEs 1 and 2 have error characteristics that are specific to each system.

Figure 4 illustrates that the first and second LLEs of the Rössler system vary intermittently. They are stationary and near the mean value for the majority of the time and then abruptly change and oscillate for a short period of time before returning to be close to the mean. This corresponds to the system trajectory being in the disc in the xy -plane, and then jumping into the “loop” with positive z -values, before returning to the disc. Predictions are extremely good in the stationary periods, and they are satisfactory during the peaks, which we label “fluctuation events”. This is particularly true for LLE 1 where we see that the ML-based predictions always catch the fluctuation event and often its sign. The predictions of LLE 2 follows similar behaviour to LLE 1, however the R^2 score suggests that the pointwise accuracy is slightly worse than for LLE 1.

On the other hand, in the Lorenz 63 system, Figure 5 shows that LLEs 1 and 2 are constantly oscillating. Certain characteristics of the target time series are well reproduced by the predictions, e.g. the largest peaks of LLE 1. These large peaks occur when the system trajectory passes close to the origin (cf. Figure 2), a region in which LLE 1 is locally homogeneous on the attractor. Nonetheless, small errors occur frequently. Notably, the higher-frequency features (such as the secondary peaks of LLE 2 between $t = 17$ and $t = 20$) are often relatively poorly reproduced for LLEs 1 and 2.

These time series provide further insight into the lower R^2 scores for LLEs 1 and 2 in the Rössler system compared to the Lorenz 63 system. Recall the definition of R^2 in Equation 15: the distance from the perfect score of 1 is the sum of squared residuals divided by the total sum of squares. The periods of stationarity in the Rössler system LLEs 1

and 2 contribute little to the total sum of squares. Consequently the larger errors during fluctuation events strongly reduce the R^2 score. In contrast, in the Lorenz 63 system, the R^2 score is high despite more frequent prediction errors because the constant variation of the target values results in a larger total sum of squares.

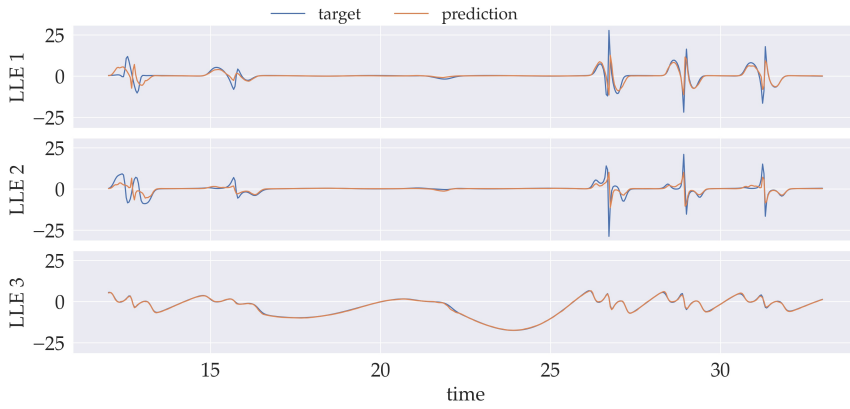


FIGURE 4 Time series of targets and predictions of test data from the Rössler system. Predictions made by an MLP with 6 input time steps. The R^2 scores for the period shown are 0.4393, 0.3175 and 0.9981 for LLEs 1, 2 and 3, respectively.

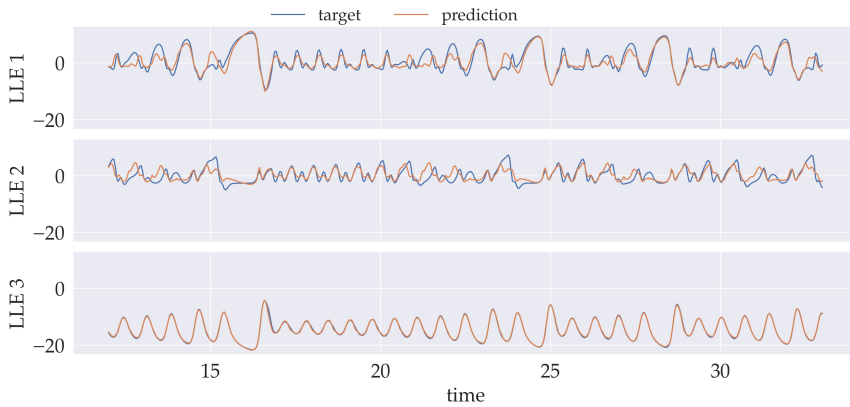


FIGURE 5 As with Figure 4 for the Lorenz 63 system. The predictions are made by a CNN with 6 input time steps. The R^2 scores for the period shown are 0.7981, 0.4897 and 0.9953 for LLEs 1, 2 and 3, respectively.

Impact of local heterogeneity in phase space

The variability of the LLEs on the strange attractor of chaotic systems is a known feature, whose immediate relevant consequence is a highly state-dependent predictability horizon: two slightly different initial conditions can generate trajectories with hugely different degree of instability. In a recent work, Lucarini and Gritsun (2020) have for the first time shown how this variability is related to the presence and distribution of unstable periodic orbits, each with

a different degree of instability, densely filling the attractor. Arbitrary solutions are bounced among these unstable periodic orbits taking their local instability features when they are in their proximity.

Recall from Section 4 that in both dynamical systems, there are regions of the system's attractor where the values of LLEs 1 and 2 are locally heterogeneous (LLE 3 is everywhere locally homogeneous). The locally heterogeneous regions in the Rössler system are in the loop with positive z -values, and in the Lorenz 63 system they form a strip that lies halfway between the outside edge and the centre of each wing. Figure 6 shows where the larger prediction errors occur on the attractor, for all configurations with a 6 time step input. More precisely, it shows the detracting from the perfect R^2 score of 1 contributed by each point. We see that for all ML algorithms, larger errors occur in the locally heterogeneous regions. Moreover, the locally heterogeneous regions are robustly difficult: for the most accurate algorithms (MLP for the Rössler system, and CNN for the Lorenz 63 system), larger prediction errors only occur in these regions. This suggests that local heterogeneity plays a key role in determining where on the attractor it is possible for ML to make reliably accurate predictions of LLEs.

Figure 7 shows that a similar pattern occurs for the absolute relative error of predictions. The relative error compares the size of the error to the size of the target value. Notably, there are some large relative errors in the locally homogeneous regions of the Rössler system attractor (*i.e.* in the disc) since the relative error is especially punitive when the target value is close to zero.

The difficulty of making accurate predictions in these regions is in line with ML theory. ML algorithms work by optimising a model (such as a NN) to approximate the map from the input to the target of the training data. ML algorithms are successful if the optimised model also approximates the map from input to target on unseen data, such as test data. This is possible only if the training data provide enough information about the unseen data. The fundamental problem in the locally heterogeneous regions is that the training data cannot provide enough information because the LLE values are noisy. In other words, the target values are highly variable even as length scales tend to zero. Thus the target values of unseen data are likely to be quite different to those of nearby seen data. Consequently, as local heterogeneity increases, ML models are less able to generalise from training data to unseen data.

The characteristics of the local heterogeneity explains the differences in prediction accuracy between the two dynamical systems. In the Rössler system, local heterogeneity in the loop of the attractor results in poorer predictions during the aforementioned fluctuation events. As explained above, errors during fluctuation events strongly reduce the R^2 score. On the other hand, in the Lorenz 63 system the values of LLEs 1 and 2 in their respective heterogeneous regions (see Figure 2) are relatively close to the mean: the largest deviations from the mean are in locally homogeneous regions. Therefore, the prediction errors resulting from locally heterogeneous regions are likely to be small compared to the deviation of the target values from the mean. Consequently, the differences in local heterogeneity explain the higher R^2 scores achieved for LLEs 1 and 2 of the Rössler system, compared to the Lorenz 63 system.

Impact of statistical distribution of targets and predictions

The poorer prediction accuracy for the Rössler system is also explained, to a lesser extent, by the statistical distribution of the LLE values. As described in Section 4, the Rössler system LLEs 1 and 2 include "extreme events", *i.e.* values of large magnitude that appear infrequently. Predicting these extreme events is very challenging for any model, and particularly so for ML: one would need to enlarge the training data set commensurately to the (very long) return times of the extreme events.

A complementary picture of the prediction accuracy is given in Figure 8 that shows target values plotted against predicted values. The panels for the first and second LLEs of the Rössler system show that all four ML algorithms fail to predict the larger magnitude targets accurately. Similarly, the QQ-plots in Figure 9 show that the predictions fail to replicate the extremities of the true values: the minimum and maximum of the predictions are lower in magnitude

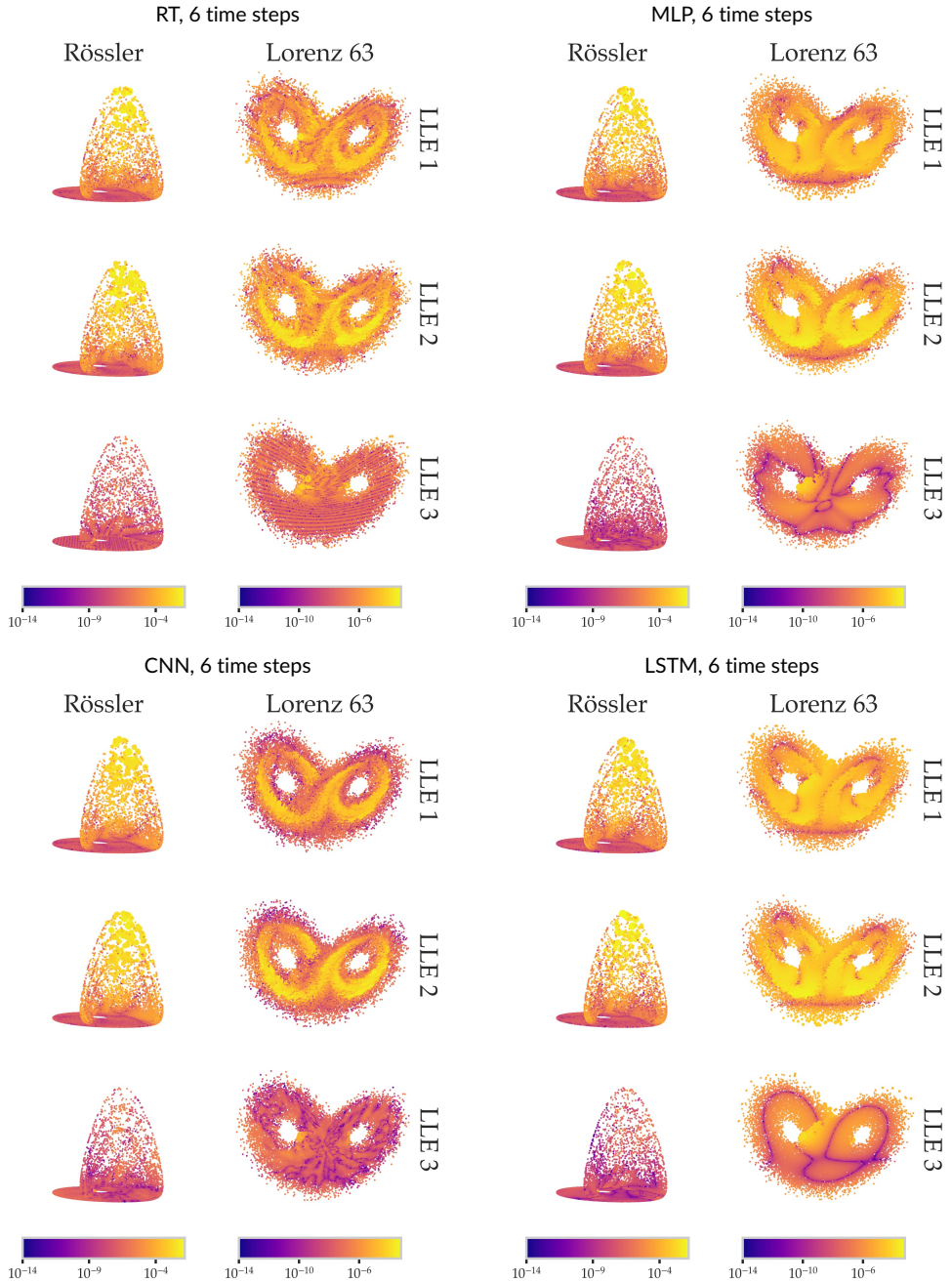


FIGURE 6 Recall the definition of the R^2 score (Equation 15): the distance from the perfect score of 1 is given by the sum of squares of residuals divided by the total sum of squares. Here we attempt to give a local (in phase space) description of the contribution towards that distance given by each prediction made on a set of 20,000 test examples. To do so we plot points that are located at the current time step x_k of the input, and both coloured and sized by the square of the residual, divided by the total sum of squares. If we denote the colour values as a_j , then $R^2 = 1 - \sum a_j$. We show all configurations with a 6 time step input. For each configuration, we use the data set instance for which the R^2 score was closest to the mean (as shown in Table 7).

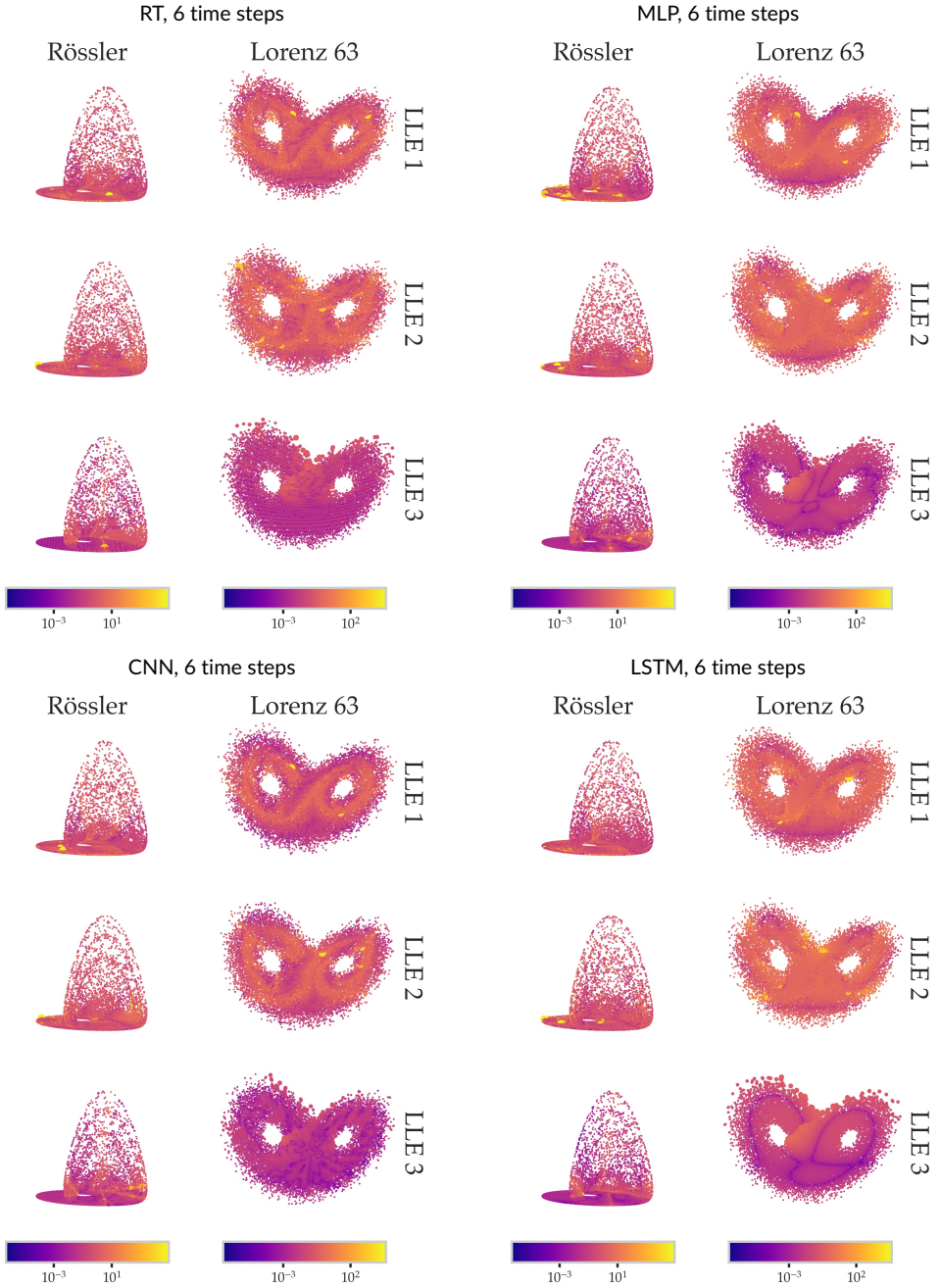


FIGURE 7 As with Figure 6, but colour and size show the location of absolute relative errors on the system attractors. The absolute relative error is given by $|y - \hat{y}| / (\epsilon + |\hat{y}|)$, where $\epsilon = 10^{-6}$, y is the prediction and \hat{y} is the target. The more yellow the point, the larger the relative error of the prediction.

than those of the target. For instance, for LLE 1, we see that the NN methods make few predictions greater than 10 in magnitude, despite target values reaching magnitudes of 25. This behaviour can also be seen in the time series plot (Figure 4). In the Lorenz 63 system, however, the larger-magnitude targets occur more frequently and are thus well-represented in the training data set. Consequently, we see in Figure 9 that the larger magnitudes are well represented in the predictions distribution, even if the predictions sometimes fail to capture the amplitude of the targets on a pointwise basis, as illustrated in Figure 5.

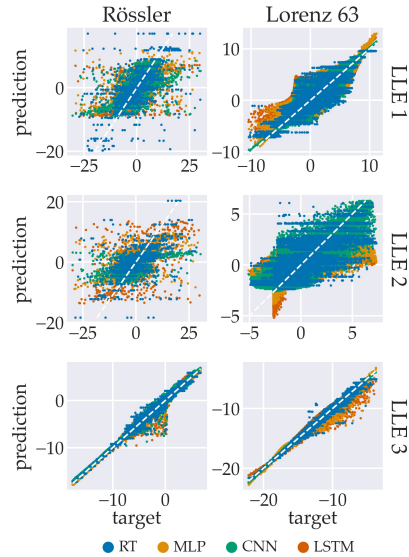


FIGURE 8 Scatter plots of targets vs. predictions, for a test data set. Note that the axis scales differ in each panel. For each method-system combination, the data are from the data set instance with R^2 closest to the mean for all data set instances. Only results from setups with 6 input time steps are shown. Note that all scatter plots show different levels of heteroskedasticity, *i.e.* the variance of a predicted value depends on the value of the target. This is a well-known challenge for regression methods.

Impact of ML approaches to exploiting temporal structure

Each of the four ML algorithms we test takes one of three approaches to exploiting the temporal structure of the input, as discussed in Section 3.2. We find that the three approaches are not equally successful across the two systems. To see this, let us focus on the configurations with 6 time steps in the input, in Table 7. In the Rössler system, the best performing ML algorithm (MLP) takes the approach of indifference to the temporal structure of the input, *i.e.*, the MLP considers each element of the input vector independently. For instance, the LLE 1 mean R^2 score for the MLP is 0.5363, slightly better than that of the LSTM (0.5319) and the CNN (0.5054) (Table 7). The second approach, learning patterns in 2-time step windows within the input, is used by the CNN. It performs worse than both the MLP and the RT in the Rössler system. The third approach consists in processing the input with an awareness of, and in order of, its time sequence, and is taken by the LSTM. Although the LSTM achieves a mean R^2 score that sits between the RT and the MLP, for LLEs 1 and 2 it is affected by a larger variability across the 30 data set instances. This suggests there is no significant advantage to ML algorithms that exploit the temporal structure (*i.e.* the second and third approaches)

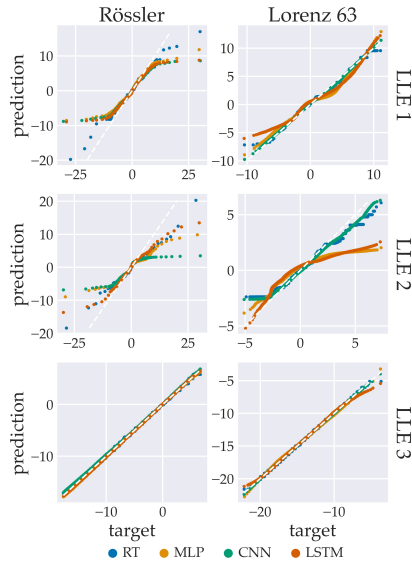


FIGURE 9 The 1000-quantiles of the predictions are plotted against those of the targets, revealing how well the two distributions match. The closer the graph to the $y = x$ line (dotted white), the closer the prediction distribution to the target distribution. Note that there is not necessarily any relationship between proximity of distributions and (point-wise) accuracy of predictions. In each panel, and for each machine learning method, the quantiles are from the test data of the data set instance with R^2 closest to the mean. Only results from setups with 6 input time steps are shown.

in the Rössler system.

In the Lorenz 63 system, the CNN is the most accurate out of the 6 time step configurations and, notably, significantly better than the other two NNs (see Table 7). Interestingly, we see that while the MLP deals poorly with the 6 time step input, the MLP with 1 time step input achieves performance very close to that of the CNN with 6 time steps. A possible explanation is that for the Lorenz 63 system, the CNN is able to exploit the pattern within the temporal structure while other NN algorithms fail to do so and are therefore negatively affected by the longer input type. For example, in the Lorenz 63 system the LSTM achieves the worst mean R^2 score of all 6 time step configurations. The 1 time step LSTM is highly variable, despite achieving mean R^2 scores similar to the RT for LLEs 1 and 3. The poor performance of the 6 time step LSTM may also be due to overfitting exacerbated by the lack of regularisation in this case (see Table 4). In other words, it may be that the hyperparameter optimisation process made a poor selection of the regularisation hyperparameter in this case. This possibility notwithstanding, the results suggest that the third approach (the LSTM) is not the best in the setting of this work. We suspect that better LSTM performance might be achieved by optimising the time steps included in the input. However, in this study we focused on comparing results achieved with one time step and multiple time steps.

We observe that among two input types we tested, the R^2 scores in Table 7 suggest there is only a small advantage to be gained by providing 6 time steps in the input rather than 1. Although the highest mean R^2 scores are achieved by configurations with 6 time step inputs, the best-scoring 1 time step configurations are not far behind.

Computation time

Table 8 shows the mean (and standard deviation) time elapsed per prediction of the three LLEs, computed over 4000 trials on a CPU processor in a personal computer. The RT is two orders of magnitude faster than the NNs. This is expected: the RT has far fewer trainable parameters (see Table 5) and, unlike the NNs, does not require the evaluation of activation functions. The RT is the only ML algorithm that is faster than the standard method of computing LLEs (propagating perturbations and orthogonalising, ignoring the time taken by the spin up iterations). Despite the comparative simplicity of the RT, it achieves R^2 scores that are close to those of the NNs. The RT does comparatively worse in the Lorenz 63 system. It is likely that the number of output values (constrained by the maximum leaf nodes hyperparameter) limited the RTs' performance more strongly in the Lorenz 63 system, due to the greater complexity of the Lorenz 63 attractor.

Execution time per set of 3 LLEs						
		Standard Method	RT	MLP	CNN	LSTM
Rössler	mean	2.32e-4	9.96e-5	2.37e-2	2.38e-2	2.34e-2
	σ	2.16e-5	3.51e-6	2.36e-2	2.57e-3	2.51e-2
Lorenz 63	mean	9.69e-4	9.88e-5	2.36e-2	2.37e-2	2.31e-1
	σ	2.53e-3	2.26e-6	2.85e-2	2.83e-2	1.60e-3

TABLE 8 The time elapsed for one set of LLEs to be calculated (by the standard method) or predicted (by the ML algorithms). The table shows the mean and standard deviation of elapsed time from 4000 trials.

6 | DISCUSSION AND SUMMARY

This study discusses the use of supervised machine learning (ML) to support numerical forecasting of chaotic dynamics. A huge amount of work has appeared recently at the crossroads between ML and the geosciences, whereby the former has provided novel data-driven solutions to complement or, in some ideal scenarios, to substitute the physical models (see *e.g.* Sonnewald et al., 2021). In this work we took a different approach that we referred to as “non intrusive”.

We did not pursue improving the given physical model with a ML model, but rather using ML models as a supplementary tool that provides information to drive adaptive decisions while running the prediction. The range of possible desirable information is ample, *e.g.* anticipating a regime change or the onset of intense convective events, as is that of consequent actions. In this work, we focused on chaotic systems where real time knowledge of the unstable properties of the system's state is of paramount relevance. Local Lyapunov exponents (LLEs) provide this knowledge in the form of the local (in time) exponential rates at which errors about the system's state evolve (Benettin et al., 1980b; Pikovsky and Politi, 2016). Nevertheless, they are notably difficult to compute, require the coding and maintaining of a tangent linear model, and the computational cost grows fast with the system's size. In this work we investigated whether supervised ML can estimate in real time the LLEs of a dynamical system trajectory based only on the system state at the current time step and a few recent time steps.

We tested four supervised ML algorithms, a regression tree (RT), a multilayer perceptron (MLP), a convolutional neural network (CNN) and a long short-term memory network (LSTM). They encompass three approaches to exploiting the temporal structure of the input. Our results indicate that the best approach is not the same for the two dynamical systems under consideration: namely, the Rössler system and the Lorenz 63 system. Both are chaotic, dissipative, 3-variable ODE systems. Overall, the results show that in certain conditions, the LLEs can be predicted well: this

depends on the system dynamics, the LLE being predicted, and importantly on the local heterogeneity of the LLE in the proximity of the given state. Our results suggest that the feasibility of using supervised ML to drive adaptive actions in an operational setting will depend on the specific use case: the forecasting model, the desired target information, and the intended adaptive actions.

The MLP performs best in the Rössler system whereas the CNN performs best in the Lorenz 63 system. The RT achieves accuracy that is close to the best-performing algorithm in both systems, whilst being computationally much cheaper than the NNs. We further show that large prediction errors occur when the current state is in a region of local heterogeneity on the system attractor. Outside of the locally heterogeneous regions, the best-performing algorithms make consistently accurate predictions. The differences in local heterogeneity between the two systems explain the lower R^2 scores achieved for LLEs 1 and 2 in the Rössler system, compared to the Lorenz 63 system. We explain that local heterogeneity is an insurmountable problem for deterministic ML predictions. This challenge could be mitigated if the ML prediction also included a reliable uncertainty quantification. We suspect that an uncertainty quantification could be made either by using Bayesian NNs (Wang and Yeung, 2016) or by including a measurement of the nearby local heterogeneity in the target of each example.

The low-dimensional setting permitted extensive experimentation in this work. The next steps will be to apply the approach of this work to spatially-extended models with more dimensions. There are several foreseeable challenges on the path from the very low-order models of this work to the envisioned setting of operational weather prediction models. The first challenge is to generate of suitable data sets, since the calculation of LLE does not scale well and requires a tangent linear model (see Section 2.2). However, the requirement of a tangent linear model can be avoided by using bred vectors (e.g. Toth and Kalnay, 1997; Uboldi and Trevisan, 2015). Additionally, the attractor of any numerical weather prediction (NWP) model is complex and high-dimensional: very large data sets will be required if sufficient attractor coverage is to be obtained. For a NWP model with $O(10^8)$ variables, one would need $O(10^{12})$ input-target pairs to obtain a ratio between the degrees of freedom of the NWP model and the size of the ML data set that is similar to the ratio used in this study. If one were to use ERA5 reanalysis data (Hersbach et al., 2020) as input, a data set of $O(10^{12})$ single time step inputs would amount to approximately $O(10^9)$ TB of data, which is unfeasibly large. Therefore, it may be necessary to operate on a reduced-resolution version of the operational model, or to curate the data sets in a strategic fashion so as to reduce their size.

The computational benefit of the ML approach investigated here is two-fold. The ML approach estimates LLEs directly from the current system state, thus avoiding the cost of the long spin up that is required by the conventional method for calculating LLEs. Second, the ML approach has the potential to be cheaper per iteration of LLEs. We found that the lightest algorithm we tested, the RT, was computationally cheaper (by a factor of 10) than the conventional method for calculating LLEs (see Table 8). Although the NNs were comparatively costly in this setting, we expect that in a higher-dimensional, operational setting, NNs will be competitive. The cost of making predictions with NNs may be improved (relative to the size of the NNs) by using purpose-built ML hardware. On the other hand, the cost of numerically calculating LLEs (by propagating perturbations and orthogonalising) will scale as $O(n^3)$ with the dimension n of the NWP model.

Acknowledgements

DA is funded by a studentship from the Engineering and Physical Sciences Research Council (EP/N509723/1). JA and AC acknowledge the support of the UK National Centre for Earth Observation (grant no. NCEO02004). AC is also supported by the project SASIP funded by Schmidt Futures – a philanthropic initiative that seeks to improve societal outcomes through the development of emerging science and technologies.

References

- Martín Abadi, Ashish Agarwal, Paul Barham, Eugene Brevdo, Zhifeng Chen, Craig Citro, Greg S. Corrado, Andy Davis, Jeffrey Dean, Matthieu Devin, Sanjay Ghemawat, Ian Goodfellow, Andrew Harp, Geoffrey Irving, Michael Isard, Yangqing Jia, Rafal Jozefowicz, Lukasz Kaiser, Manjunath Kudlur, Josh Levenberg, Dandelion Mané, Rajat Monga, Sherry Moore, Derek Murray, Chris Olah, Mike Schuster, Jonathon Shlens, Benoit Steiner, Ilya Sutskever, Kunal Talwar, Paul Tucker, Vincent Vanhoucke, Vijay Vasudevan, Fernanda Viégas, Oriol Vinyals, Pete Warden, Martin Wattenberg, Martin Wicke, Yuan Yu, and Xiaoqiang Zheng. TensorFlow: Large-scale machine learning on heterogeneous systems, 2015. URL <https://www.tensorflow.org/>. Software available from tensorflow.org. 10
- Aishah Albarakati, Marko Budišić, Rose Crocker, Juniper Glass-Klaiber, Sarah Iams, John Maclean, Noah Marshall, Colin Roberts, and Erik S. Van Vleek. Model and data reduction for data assimilation: Particle filters employing projected forecasts and data with application to a shallow water model. *Computers & Mathematics with Applications*, 2021. ISSN 0898-1221. doi: <https://doi.org/10.1016/j.camwa.2021.05.026>. URL <https://www.sciencedirect.com/science/article/pii/S0898122121002121>. 3
- Martin Albrecht, Gregory Bard, and William Hart. Algorithm 898: Efficient multiplication of dense matrices over $gf(2)$. *ACM Trans. Math. Softw.*, 37(1), January 2010. ISSN 0098-3500. doi: [10.1145/1644001.1644010](https://doi.org/10.1145/1644001.1644010). URL <https://doi.org/10.1145/1644001.1644010>. 8
- Josh Alman and Virginia Vassilevska Williams. A Refined Laser Method and Faster Matrix Multiplication. In *Proceedings of the 2021 ACM-SIAM Symposium on Discrete Algorithms (SODA)*, pages 522–539. Society for Industrial and Applied Mathematics, Philadelphia, PA, Jan 2021. doi: [10.1137/1.9781611976465.32](https://doi.org/10.1137/1.9781611976465.32). URL <http://arxiv.org/abs/2010.05846><https://epubs.siam.org/doi/10.1137/1.9781611976465.32>. 8
- Peter Arbenz. The QR Algorithm. In *Lecture notes on Numerical Methods for Solving Large Scale Eigenvalue Problems*, pages 63-90, 2016. Available at <http://people.inf.ethz.ch/arbenz/ewp/lnotes.html>, accessed 2021/06/20, 2016. 8
- Giancarlo Benettin, Luigi Galgani, Antonio Giorgilli, and Jean-Marie Strelcyn. Lyapunov Characteristic Exponents for smooth dynamical systems and for hamiltonian systems; a method for computing all of them. Part 2: Numerical application. *Meccanica*, 15:21–30, Mar 1980a. doi: [10.1007/BF02128237](https://doi.org/10.1007/BF02128237). URL <http://link.springer.com/10.1007/BF02128236>. 3, 4, 7
- Giancarlo Benettin, Luigi Galgani, Antonio Giorgilli, and Jean-Marie Strelcyn. Lyapunov Characteristic Exponents for smooth dynamical systems and for hamiltonian systems; a method for computing all of them. Part 1: Theory. *Meccanica*, 15:9–20, Mar 1980b. ISSN 0025-6455. doi: [10.1007/BF02128236](https://doi.org/10.1007/BF02128236). URL <http://link.springer.com/10.1007/BF02128236>. 3, 4, 7, 26
- Christopher M. Bishop. *Neural networks for pattern recognition*. Clarendon Press, Oxford, 1995. 2, 3
- Marc Bocquet, Karthik S. Gurumoorthy, Amit Apte, Alberto Carrassi, Colin Grudzien, and Christopher K. R. T. Jones. Degenerate kalman filter error covariances and their convergence onto the unstable subspace. *SIAM/ASA Journal on Uncertainty Quantification*, 5(1):304–333, 2017. doi: [10.1137/16M1068712](https://doi.org/10.1137/16M1068712). URL <https://doi.org/10.1137/16M1068712>. 17
- Thomas Bolton and Laure Zanna. Applications of deep learning to ocean data inference and subgrid parameterization. *Journal of Advances in Modeling Earth Systems*, 11(1):376–399, 2019. doi: <https://doi.org/10.1029/2018MS001472>. URL <https://agupubs.onlinelibrary.wiley.com/doi/abs/10.1029/2018MS001472>. 3
- Massimo Bonavita and Patrick Laloyaux. Machine Learning for Model Error Inference and Correction. *Journal of Advances in Modeling Earth Systems*, 12(12), Dec 2020. ISSN 1942-2466. doi: [10.1029/2020MS002232](https://doi.org/10.1029/2020MS002232). URL <https://onlinelibrary.wiley.com/doi/10.1029/2020MS002232>. 3
- Julien Brajard, Alberto Carrassi, Marc Bocquet, and Laurent Bertino. Combining data assimilation and machine learning to emulate a dynamical model from sparse and noisy observations: a case study with the lorenz 96 model. *Journal of Computational Science*, 44:101171, 2020. 3

- Julien Brajard, Alberto Carrassi, Marc Bocquet, and Laurent Bertino. Combining data assimilation and machine learning to infer unresolved scale parametrization. Philosophical Transactions of the Royal Society A: Mathematical, Physical and Engineering Sciences, 379(2194):20200086, Apr 2021. doi: 10.1098/rsta.2020.0086. URL <https://royalsocietypublishing.org/doi/10.1098/rsta.2020.0086>. 3
- L. Breiman, J. Friedman, C.J. Stone, and R.A. Olshen. Classification and Regression Trees. Taylor & Francis, 1984. doi: 10.1201/9781315139470. 4, 9
- Roberto Buizza. Introduction to the special issue on “25 years of ensemble forecasting”. Quarterly Journal of the Royal Meteorological Society, 145:1–11, 2019. 3
- Alberto Carrassi, Marc Bocquet, Jonathan Demaeyer, Colin Grudzien, Patrick Raanes, and Stéphane Vannitsem. Data assimilation for chaotic dynamics. In Seon Ki Park and Liang Xu, editors, Data Assimilation for Atmospheric, Oceanic and Hydrologic Applications (Vol. IV), pages 1–42. Springer International Publishing, Cham, 2022. ISBN 978-3-030-77722-7. doi: 10.1007/978-3-030-77722-7_1. URL https://doi.org/10.1007/978-3-030-77722-7_1. 3
- Matthew Chantry, Hannah Christensen, Peter Dueben, and Tim Palmer. Opportunities and challenges for machine learning in weather and climate modelling: hard, medium and soft AI. Philosophical Transactions of the Royal Society A: Mathematical, Physical and Engineering Sciences, 379(2194):20200083, April 2021. doi: 10.1098/rsta.2020.0083. URL <https://royalsocietypublishing.org/doi/10.1098/rsta.2020.0083>. 3
- Y. Chen, A. Carrassi, and V. Lucarini. Inferring the instability of a dynamical system from the skill of data assimilation exercises. Nonlinear Processes in Geophysics, 28(4):633–649, 2021. doi: 10.5194/npg-28-633-2021. URL <https://npg.copernicus.org/articles/28/633/2021/>. 3
- Peter Düben, Umberto Modigliani, Alan Geer, Stephan Siemen, Florian Pappenberger, Peter Bauer, Andy Brown, Martin Palkovic, Baudouin Raoult, Nils Wedi, and Vasileios Baousis. Machine learning at ecmwf: A roadmap for the next 10 years. Technical Report 878, ECMWF, 01 2021. URL <https://www.ecmwf.int/node/19877>. 3
- Ronan Fablet, Said Ouala, and Cedric Herzet. Bilinear Residual Neural Network for the Identification and Forecasting of Geophysical Dynamics. In 2018 26th European Signal Processing Conference (EUSIPCO), pages 1477–1481. IEEE, Sep 2018. doi: 10.23919/EUSIPCO.2018.8553492. URL <https://ieeexplore.ieee.org/document/8553492/>. 3
- Michael Ghil and Valerio Lucarini. The physics of climate variability and climate change. Rev. Mod. Phys., 92:035002, Jul 2020. doi: 10.1103/RevModPhys.92.035002. URL <https://link.aps.org/doi/10.1103/RevModPhys.92.035002>. 2
- Gene H. Golub and Charles F. Van Loan. Matrix Computations. Johns Hopkins University Press, Baltimore, MD, 4th edition, 2013. URL <https://jhupbooks.press.jhu.edu/title/matrix-computations>. 7, 8
- Ian Goodfellow, Yoshua Bengio, and Aaron Courville. Deep Learning. MIT Press, 2016. <http://www.deeplearningbook.org>. 4, 9, 14
- Georg A. Gottwald and Sebastian Reich. Supervised learning from noisy observations: Combining machine-learning techniques with data assimilation. Physica D: Nonlinear Phenomena, 423:132911, Sep 2021. ISSN 01672789. doi: 10.1016/j.physd.2021.132911. URL <https://linkinghub.elsevier.com/retrieve/pii/S0167278921000695>. 3
- Alex Graves. Long Short-Term Memory. In Supervised Sequence Labelling with Recurrent Neural Networks. Studies in Computational Intelligence, vol 385., pages 37–45. Springer Berlin Heidelberg, 2012. doi: 10.1007/978-3-642-24797-2_4. URL http://link.springer.com/10.1007/978-3-642-24797-2_{_}4. 4, 10
- Alex Graves, Abdel-Rahman Mohamed, and Geoffrey Hinton. Speech recognition with deep recurrent neural networks. In 2013 IEEE International Conference on Acoustics, Speech and Signal Processing, pages 6645–6649, 2013. doi: 10.1109/ICASSP.2013.6638947. 10
- Trevor Hastie, Robert Tibshirani, and Jerome Friedman. The Elements of Statistical Learning. Springer, New York, NY, 2009. doi: <https://doi.org/10.1007/978-0-387-84858-7>. 2, 3, 14

- Tim Head, Manoj Kumar, Holger Nahrstaedt, Gilles Louppe, and Iaroslav Shcherbatyi. *scikit-optimize/scikit-optimize*, October 2021. URL <https://doi.org/10.5281/zenodo.5565057>. 14
- Hans Hersbach, Bill Bell, Paul Berrisford, Shoji Hirahara, András Horányi, Joaquín Muñoz-Sabater, Julien Nicolas, Carole Peubey, Raluca Radu, Dinand Schepers, Adrian Simmons, Cornel Soci, Saleh Abdalla, Xavier Abellan, Gianpaolo Balsamo, Peter Bechtold, Gionata Biavati, Jean Bidlot, Massimo Bonavita, Giovanna De Chiara, Per Dahlgren, Dick Dee, Michail Diamantakis, Rossana Dragani, Johannes Flemming, Richard Forbes, Manuel Fuentes, Alan Geer, Leo Haimberger, Sean Healy, Robin J. Hogan, Elías Hólm, Marta Janisková, Sarah Keeley, Patrick Laloyaux, Philippe Lopez, Cristina Lupu, Gabor Radnoti, Patricia de Rosnay, Iryna Rozum, Freja Vamborg, Sebastien Villaume, and Jean-Noël Thépaut. The era5 global reanalysis. *Quarterly Journal of the Royal Meteorological Society*, 146(730):1999–2049, 2020. doi: <https://doi.org/10.1002/qj.3803>. URL <https://rmets.onlinelibrary.wiley.com/doi/abs/10.1002/qj.3803>. 27
- Sepp Hochreiter and Jürgen Schmidhuber. Long Short-Term Memory. *Neural Computation*, 9(8):1735–1780, Nov 1997. ISSN 0899-7667. doi: 10.1162/neco.1997.9.8.1735. URL <https://www.mitpressjournals.org/doi/abs/10.1162/neco.1997.9.8.1735><https://direct.mit.edu/neco/article/9/8/1735-1780/6109>. 4, 10
- James R. Holton and Gregory J. Hakim. *An Introduction to Dynamic Meteorology*. Elsevier, 2013. doi: 10.1016/C2009-0-63394-8. 2
- Arieh Iserles. Magnus expansions and beyond. In Kurusch Ebrahimi-Fard, Matilde Marcolli, and Walter D. van Suijlekom, editors, *Combinatorics and Physics*, volume 539, pages 171–186. American Mathematical Society, 2011. doi: 10.1090/conm/539/10634. URL <http://www.ams.org/conm/539/>. 5
- James L. Kaplan and James A. Yorke. Chaotic behavior of multidimensional difference equations. In Heinz-Otto Peitgen and Hans-Otto Walther, editors, *Functional Differential Equations and Approximation of Fixed Points*, pages 204–227, Berlin, Heidelberg, 1979. Springer Berlin Heidelberg. 3
- Pavel V. Kuptsov and Ulrich Parlitz. Theory and Computation of Covariant Lyapunov Vectors. *Journal of Nonlinear Science*, 22(5):727–762, Oct 2012. ISSN 0938-8974. doi: 10.1007/s00332-012-9126-5. URL <http://link.springer.com/10.1007/s00332-012-9126-5>. 3, 4, 6, 7, 8, 17
- Yann LeCun, Bernhard Boser, John Denker, Donnie Henderson, R. Howard, Wayne Hubbard, and Lawrence Jackel. Handwritten digit recognition with a back-propagation network. In D. Touretzky, editor, *Advances in Neural Information Processing Systems*, volume 2. Morgan-Kaufmann, 1990. URL <https://proceedings.neurips.cc/paper/1989/file/53c3bce66e43be4f209556518c2fcb54-Paper.pdf>. 4, 10
- B Legras and R Vautard. A Guide To Liapunov Vectors. In Tim Palmer, editor, *Seminar on Predictability*, volume 1, pages 135–146, Reading, UK, 1996. ECMWF. URL <https://www.ecmwf.int/en/learning/workshops-and-seminars/past-workshops/1995-annual-seminar>. 4, 5
- James Lighthill, J M T Thompson, A K Sen, A G M Last, D T Tritton, and P Mathias. The Recently Recognized Failure of Predictability in Newtonian Dynamics [and Discussion]. *Proceedings of the Royal Society of London. Series A, Mathematical and Physical Sciences*, 407(1832):35–50, May 1986. ISSN 00804630. URL <http://www.jstor.org/stable/2397780>. 2
- Edward N. Lorenz. Deterministic Nonperiodic Flow. *Journal of the Atmospheric Sciences*, 20(2):130–141, Mar 1963. ISSN 0022-4928. doi: 10.1175/1520-0469(1963)020<0130:DNF>2.0.CO;2. URL [http://journals.ametsoc.org/doi/10.1175/1520-0469\(1963\)020\(3C0130:DNF\)3E2.0.CO;2](http://journals.ametsoc.org/doi/10.1175/1520-0469(1963)020(3C0130:DNF)3E2.0.CO;2). 11
- Valerio Lucarini and Andrey Gritsun. A new mathematical framework for atmospheric blocking events. *Climate Dynamics*, 54(1):575–598, 2020. 13, 20
- National Institute of Standards and Technology (U.S.). Nist/sematech e-handbook of statistical methods, 2012. URL <https://www.itl.nist.gov/div898/handbook/eda/section3/qplot.htm>. [Online; accessed 21-December-2021]. 9

- Duong Nguyen, Said Ouala, Lucas Drumetz, and Ronan Fablet. EM-like Learning Chaotic Dynamics from Noisy and Partial Observations, 2019. 3
- Duong Nguyen, Said Ouala, Lucas Drumetz, and Ronan Fablet. Variational deep learning for the identification and reconstruction of chaotic and stochastic dynamical systems from noisy and partial observations, 2021. 3
- Paul A. O’Gorman and John G. Dwyer. Using Machine Learning to Parameterize Moist Convection: Potential for Modeling of Climate, Climate Change, and Extreme Events. *Journal of Advances in Modeling Earth Systems*, 10(10):2548–2563, Oct 2018. ISSN 1942-2466. doi: 10.1029/2018MS001351. URL <https://onlinelibrary.wiley.com/doi/10.1029/2018MS001351>. 3
- Valery Oseledets. A multiplicative ergodic theorem. Lyapunov characteristic numbers for dynamical systems. *Trans. Moscow Math. Soc.*, 19:197–231, 1968. 6
- Edward Ott. *Chaos in Dynamical Systems*. Cambridge University Press, 2 edition, 2002. doi: 10.1017/CBO9780511803260. 2, 11
- Luigi Palatella, Alberto Carrassi, and Anna Trevisan. Lyapunov vectors and assimilation in the unstable subspace: theory and applications. *Journal of Physics A: Mathematical and Theoretical*, 46(25):254020, 2013. 3
- T. N. Palmer. Predictability of the atmosphere and oceans: From days to decades. In David L. T. Anderson and Jürgen Willebrand, editors, *Decadal Climate Variability*, pages 83–155, Berlin, Heidelberg, 1996. Springer Berlin Heidelberg. 2
- Dhruvit Patel, Daniel Canaday, Michelle Girvan, Andrew Pomerance, and Edward Ott. Using machine learning to predict statistical properties of non-stationary dynamical processes: System climate, regime transitions, and the effect of stochasticity. *Chaos: An Interdisciplinary Journal of Nonlinear Science*, 31(3):033149, Mar 2021. ISSN 1054-1500. doi: 10.1063/5.0042598. URL <https://aip.scitation.org/doi/10.1063/5.0042598>. 3
- Jaideep Pathak, Zhixin Lu, Brian R. Hunt, Michelle Girvan, and Edward Ott. Using machine learning to replicate chaotic attractors and calculate lyapunov exponents from data. *Chaos: An Interdisciplinary Journal of Nonlinear Science*, 27(12):121102, Dec 2017. ISSN 1089-7682. doi: 10.1063/1.5010300. URL <http://dx.doi.org/10.1063/1.5010300>. 3
- Jaideep Pathak, Brian Hunt, Michelle Girvan, Zhixin Lu, and Edward Ott. Model-Free Prediction of Large Spatiotemporally Chaotic Systems from Data: A Reservoir Computing Approach. *Physical Review Letters*, 120(2):024102, Jan 2018. ISSN 0031-9007. doi: 10.1103/PhysRevLett.120.024102. URL <https://link.aps.org/doi/10.1103/PhysRevLett.120.024102>. 3
- F. Pedregosa, G. Varoquaux, A. Gramfort, V. Michel, B. Thirion, O. Grisel, M. Blondel, P. Prettenhofer, R. Weiss, V. Dubourg, J. Vanderplas, A. Passos, D. Cournapeau, M. Brucher, M. Perrot, and E. Duchesnay. Scikit-learn: Machine learning in Python. *Journal of Machine Learning Research*, 12:2825–2830, 2011. 11
- Arkady Pikovsky and Antonio Politi. *Lyapunov Exponents*. Cambridge University Press, Cambridge, 2016. doi: 10.1017/CBO9781139343473. URL <http://ebooks.cambridge.org/ref/id/CBO9781139343473>. 2, 3, 4, 5, 6, 7, 11, 26
- K. Ramasubramanian and M.S. Sriram. A comparative study of computation of Lyapunov spectra with different algorithms. *Physica D: Nonlinear Phenomena*, 139(1-2):72–86, May 2000. ISSN 01672789. doi: 10.1016/S0167-2789(99)00234-1. URL <https://linkinghub.elsevier.com/retrieve/pii/S0167278999002341>. 7
- Stephan Rasp. Coupled online learning as a way to tackle instabilities and biases in neural network parameterizations: general algorithms and Lorenz 96 case study (v1.0). *Geoscientific Model Development*, 13(5):2185–2196, May 2020. ISSN 1991-9603. doi: 10.5194/gmd-13-2185-2020. URL <https://gmd.copernicus.org/articles/13/2185/2020/>. 3
- Stephan Rasp, Michael S. Pritchard, and Pierre Gentine. Deep learning to represent subgrid processes in climate models. *Proceedings of the National Academy of Sciences*, 115(39):9684–9689, Sep 2018. ISSN 0027-8424. doi: 10.1073/pnas.1810286115. URL <http://www.pnas.org/lookup/doi/10.1073/pnas.1810286115>. 3

- Stephan Rasp, Peter D. Dueben, Sebastian Scher, Jonathan A. Weyn, Soukayna Mouatadid, and Nils Thuerey. WeatherBench: A Benchmark Data Set for Data-Driven Weather Forecasting. Journal of Advances in Modeling Earth Systems, 12(11), Nov 2020. ISSN 1942-2466. doi: 10.1029/2020MS002203. URL <https://onlinelibrary.wiley.com/doi/10.1029/2020MS002203>. 3
- Markus Reichstein, Gustau Camps-Valls, Bjorn Stevens, Martin Jung, Joachim Denzler, Nuno Carvalhais, and Prabhat. Deep learning and process understanding for data-driven Earth system science. Nature, 566(7743):195–204, 2019. ISSN 14764687. doi: 10.1038/s41586-019-0912-1. URL <http://dx.doi.org/10.1038/s41586-019-0912-1>. 3
- O.E. Rössler. An equation for continuous chaos. Physics Letters A, 57(5):397–398, Jul 1976. ISSN 03759601. doi: 10.1016/0375-9601(76)90101-8. URL <https://linkinghub.elsevier.com/retrieve/pii/0375960176901018>. 11
- David Ruelle. Ergodic theory of differentiable dynamical systems. Publications Mathématiques de l'IHÉS, 50:27–58, 1979. URL http://www.numdam.org/item/PMIHES_1979__50__27_0/. 6
- Marco Sandri. Numerical calculation of Lyapunov exponents. Mathematica Journal, 6(3):78–84, 1996. ISSN 1047-5974. 3, 7
- M. G. Schultz, C. Betancourt, B. Gong, F. Kleinert, M. Langguth, L. H. Leufen, A. Mozaffari, and S. Stadler. Can deep learning beat numerical weather prediction? Philosophical Transactions of the Royal Society A: Mathematical, Physical and Engineering Sciences, 379(2194):20200097, Apr 2021. doi: 10.1098/rsta.2020.0097. URL <https://royalsocietypublishing.org/doi/10.1098/rsta.2020.0097>. 3
- Yakov Sinai. Kolmogorov-Sinai entropy. Scholarpedia, 4(3):2034, 2009. ISSN 1941-6016. doi: 10.4249/scholarpedia.2034. URL <http://www.scholarpedia.org/article/Kolmogorov-Sinai{ }entropy>. 3
- Jasper Snoek, Hugo Larochelle, and Ryan P. Adams. Practical bayesian optimization of machine learning algorithms. In Proceedings of the 25th International Conference on Neural Information Processing Systems - Volume 2, NIPS'12, pages 2951–2959, 2012. 14
- Maike Sonnewald, Redouane Lguensat, Daniel C Jones, Peter D Dueben, Julien Brajard, and V Balaji. Bridging observations, theory and numerical simulation of the ocean using machine learning. Environmental Research Letters, 16(7):073008, jul 2021. doi: 10.1088/1748-9326/ac0eb0. 3, 26
- Gilbert Strang. Introduction to Linear Algebra. Wellesley-Cambridge Press, 5th edition, 2016. 7
- Steven H. Strogatz. Nonlinear Dynamics and Chaos. CRC Press, May 2018. doi: 10.1201/9780429492563. URL <https://www.taylorfrancis.com/books/9780429961113>. 4
- Z. Toth and E. Kalnay. Ensemble Forecasting at NCEP and the Breeding Method. Monthly Weather Review, 12(125):3297–3319, 1997. URL [https://doi.org/10.1175/1520-0493\(1997\)125<3297:EFANAT>2.0.CO;2](https://doi.org/10.1175/1520-0493(1997)125<3297:EFANAT>2.0.CO;2). 3, 27
- F. Uboldi and A. Trevisan. Multiple-scale error growth in a convection-resolving model. Nonlinear Processes in Geophysics, 22(1):1–13, 2015. doi: 10.5194/npg-22-1-2015. URL <https://npg.copernicus.org/articles/22/1/2015/>. 27
- Stéphane Vannitsem. Predictability of large-scale atmospheric motions: Lyapunov exponents and error dynamics. Chaos: An Interdisciplinary Journal of Nonlinear Science, 27(3):032101, Mar 2017. ISSN 1054-1500. doi: 10.1063/1.4979042. URL <http://aip.scitation.org/doi/10.1063/1.4979042>. 2, 13
- Stéphane Vannitsem and Wansuo Duan. On the use of near-neutral backward lyapunov vectors to get reliable ensemble forecasts in coupled ocean-atmosphere systems. Climate Dynamics, 55:1125–1139, 2020. 3
- Hao Wang and Dit-Yan Yeung. Towards bayesian deep learning: A framework and some existing methods. IEEE Transactions on Knowledge and Data Engineering, 28(12):3395–3408, 2016. doi: 10.1109/TKDE.2016.2606428. 27
- M. B. Wilk and R. Gnanadesikan. Probability plotting methods for the analysis for the analysis of data. Biometrika, 55(1):1–17, 03 1968. doi: 10.1093/biomet/55.1.1. URL <https://doi.org/10.1093/biomet/55.1.1.9>

Alan Wolf, Jack B. Swift, Harry L. Swinney, and John A. Vastano. Determining Lyapunov exponents from a time series. Physica D: Nonlinear Phenomena, 16(3):285–317, 1985. doi: [https://doi.org/10.1016/0167-2789\(85\)90011-9](https://doi.org/10.1016/0167-2789(85)90011-9). 6

Yonghui Wu, Mike Schuster, Zhifeng Chen, Quoc V. Le, Mohammad Norouzi, Wolfgang Macherey, Maxim Krikun, Yuan Cao, Qin Gao, Klaus Macherey, Jeff Klingner, Apurva Shah, Melvin Johnson, Xiaobing Liu, Łukasz Kaiser, Stephan Gouws, Yoshikiyo Kato, Taku Kudo, Hideto Kazawa, Keith Stevens, George Kurian, Nishant Patil, Wei Wang, Cliff Young, Jason Smith, Jason Riesa, Alex Rudnick, Oriol Vinyals, Greg Corrado, Macduff Hughes, and Jeffrey Dean. Google's neural machine translation system: Bridging the gap between human and machine translation, 2016. 10